A Search for Supernova Light Echoes in NGC 6946 with SITELLE

A Search for Supernova Light Echoes in NGC 6946 with SITELLE

By Michael Radica, B.Sc.

A Thesis Submitted to the School of Graduate Studies in the Partial Fulfillment of the Requirements for the Degree Master of Science

McMaster University

Master of Science (2019)

Hamilton, Ontario (Physics & Astronomy)

TITLE: A Search for Supernova Light Echoes in NGC 6946 with SITELLE

AUTHOR: Michael Radica (McMaster University)

SUPERVISOR: Dr. Douglas Welch

NUMBER OF PAGES: ix, 88

Abstract

Scattered light echoes provide a unique way to engage in late-time study of supernovae. Formed when light from a supernova scatters off of nearby dust, and arrives at Earth long after the supernova has initially faded from the sky, light echoes can be used to study the precursor supernova through both photometric and spectroscopic methods. The detection rate of light echoes, especially from Type II supernovae, is not well understood, and large scale searches are confounded by uncertainties in supernova ages and peak luminosities.

We provide a novel spectroscopic search method for detecting light echoes, and test it with 4 hours of observations of NGC 6946 using the SITELLE Imaging Fourier Transform Spectrometer mounted on the Canada-France-Hawaii Telescope. Our procedure relies on fitting a sloped model to continuum emission, and identifying negatively-sloped continua with the downslope of the emission component of a highly-broadened P-Cygni profile in the Hα line, characteristic of supernova ejecta.

We find no clear evidence for light echoes from any of the ten known Type II supernovae in NGC 6946, and only one light echo candidate from potential historical supernovae predating 1917. We do however, present an upper limit in Hα brightness of $5 \times 10^{-17}\,\mathrm{erg/s/cm^2/arcsec^2}$ for light echoes within this galaxy. We discuss extensions of our methodology, as well as viability of this type of study in other objects, and with other instruments.

Acknowledgements

I first must thank Doug Welch for having the many qualities that make a great advisor: knowing when I needed some encouragement, when I needed a push, and always being ready with a good joke. I also need to thank Laurie Rousseau-Nepton, and Simon Prunet. Without your expertise, this project would not have been possible.

I am thankful to my committee members: Laura Parker, and Alison Sills for being mentors throughout both my graduate, and undergraduate studies. This will be the culmination of my seven years at McMaster, and I owe my thanks to everyone in the department, and especially in 201, who made McMaster feel like home.

Lastly, to my family for telling me to 'keep up the hard work', and to Abbey and Teddy for being there when I need it most.

Contents

List of Figures

List of Tables

Chapter 1

Introduction

1.1 Supernovae

There is arguably no class of events in the universe that are more influential than supernovae (SNe), both physically and scientifically. The mechanisms powering a supernova (SN) are strong functions of the mass of the progenitor star. Although specific subclassifications depend on the shape of the light curve and presence of spectral lines, SNe can generally be divided into two distinct categories: core-collapse, and thermonuclear explosions.

Thermonuclear SNe, most commonly of Type Ia, have remarkably similar light curves and spectra, which possess no Hydrogen or Helium lines (Arnett & Truran, 1969, Hillebrandt & Niemeyer, 2000). They are thought to be the explosions of one single class of stars: Carbon-Oxygen white dwarfs (CO WDs) (Nugent et al., 2011). The most likely mechanism behind such events is the presence of a CO WD in a binary system with another main sequence (MS), or post-MS star (Whelan & Iben Jr, 1973). The WD can accrete material from its companion star until its total mass reaches the Chandrasekhar limit; $1.4\,\mathrm{M}_{\odot}$. At this point, the degenerate material in the CO WD begins runaway Carbon burning resulting in a thermonuclear explosion. Type Ia SNe can also occur from a double degenerate scenario, whereby two WDs collide - causing the total stellar mass to exceed the Chandrasekhar limit and initiate the thermonuclear explosion (Whipple, 1939, Van Kerkwijk et al., 2010).

Type Ia SNe have been of extraordinary use to astronomers due to their ability to be used as standard candles (Phillips, 1993). Measurements of distances to galaxies containing Type Ia SNe led directly to the discovery of the accelerating expansion of the universe, and the importance of "dark energy" (Riess et al., 1998, Perlmutter et al., 1999).

Much more massive stars, in the range of $140\,\mathrm{M}_\odot$ to $260\,\mathrm{M}_\odot$, can also end their stellar lives in a thermonuclear explosion initiated by electron-positron pair instability in their cores (Barkat et al., 1967, Woosley et al., 2002). These stars generally have extremely massive Helium cores, in which electron-positron annihilation can ignite Oxygen and Silicon burning in the envelope. The ensuing thermonuclear explosion completely destroys the star, leaving behind no remnant (Fryer & Kalogera, 2001). These SNe can be distinguished from the classical Type Ia by their longer lasting, and more energetic explosions (Kasen et al., 2011).

The second category, core-collapse SNe, are the end-of-life events for stars with masses $8\,\mathrm{M}_\odot < \mathrm{M} < 140\,\mathrm{M}_\odot$ (Smartt, 2009). Such stars undergo stages of nuclear fusion culminating in a degenerate core composed mainly of Iron (Nomoto, 1987). The core so created is unable to produce energy from nuclear fusion, sapping the pressure support of the star and leading to a collapse driven by gravitational instability. Current models of nucleosynthesis predict that the elements of Carbon through to Iron are formed through nuclear fusion in the cores of massive stars, and core-collapse events are one method of distributing these elements throughout the universe (Burbidge et al., 1957). Furthermore, some elements heavier than Iron, such as Krypton and Bromine, are formed through r-process nucleosynthesis in the SN explosion itself (Seeger et al., 1965).

Core-collapse SNe can be of either Type II, or Type Ib/Ic, depending on the presence of Hydrogen lines in their spectra. During the latter stages of their lives, stars with masses greater than $25\,\mathrm{M}_\odot$ can have violent stellar winds and experience mass loss of

$\sim 10^{-5}\,M_{\odot}$/year (Dray et al., 2003). If such a star has shed its entire Hydrogen envelope prior to becoming a SN, the lack of Hydrogen lines in its spectrum will result in Type Ib classification. If the star has also shed its Helium, the SN will be of Type Ic (Filippenko, 2004). If Hydrogen lines are present in the SN spectrum, it is of Type II.

Unlike thermonuclear SNe which leave no remnant, the result of a core-collapse SN is generally a neutron star (NS), or a black hole (BH) (Nomoto, 1987; Canal & Schatzman, 1976). Sub-classification of Type II SNe are based on a combination of spectra at maximum light, and light curve shape. Table 1.1, based on results from Li et al. (2011), lists the main classifications of core-collapse SNe, as well as some characteristic features in their spectra and light curves.

Table 1.1: Classification of core-collapse SNe based on features of their light curves and spectra.

Class	Spectrum	Light Curve
Ib	No H	-
Ic	No H or He	-
IIP	-	Plateau in light curve
IIL	-	Linear drop off in light curve
IIb	Weak H line	-
IIn	Narrow H line	-

This study is predominantly an Hα survey, and would not be able to detect emission from SNe of Type I. Therefore, it is only SNe of Type II that we will be concerned with throughout the remainder of this thesis.

1.2 Supernova Light Echoes

The timescales over which SNe evolve are unusually short compared to many astronomical objects - they change dramatically on human and historical timescales. During an eruption, the energy output of a SN can rival that of their entire host galaxy. However, it will only remain visible in the sky for a few weeks or months, after which we can no longer observe the SN itself, only the remnant. Supernova light echoes (SN LEs), formed when scattered light from a SN reaches Earth, are a unique way to study SNe long after direct light from the event has passed.

The first LE was serendipitously discovered in November 1901 by George Ritchey as a nebular brightness around Nova Persei 1901 - although at the time the idea of a LE was yet unknown (Ritchey, 1901). Further analysis by Kapteyn (1901) deduced that the nebulosity Ritchey observed was merely an illumination of dust rather than a unique object in and of itself. Finally Couderc (1939) formulated the geometry that led to the recognition of Ritchey's discovery as the first ever scattered LE system.

1.2.1 Light Echo Geometry

The geometry proposed by Couderc (1939) to explain the Nova Persei 1901 LE is summarized in Figure 1.1.

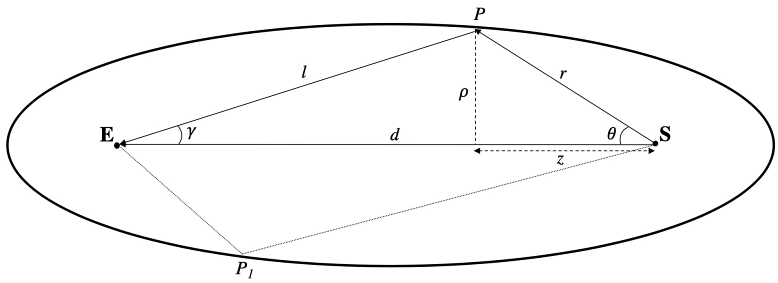

FIGURE 1.1: Geometry of a scattered LE in two-dimensions as proposed by Couderc (1939). A LE from source event S could be seen from Earth (E) at any point on the echo-ellipse (e.g. P, P_1), which is constructed with Earth and the source at either focus. In three-dimensions, the echo-ellipse becomes an ellipsoid. Notation is adapted from Tylenda (2004).

Following the formalism of Tylenda (2004), consider some transient source event observed at position S at time t_0, and a LE observed from this event at time t_e, at position P. Furthermore, let d be the distance from the source event to Earth, r be the distance from the source event to some scattering material (e.g. a dust cloud), and l be the distance to the scattering material from Earth. We will also define the delay time,

t, such that $t = t_e - t_0$ is the time between the observation of the source event, and the detection of the LE. Therefore, by the geometry laid out in Figure 1.1, the scattered light has travelled an additional distance

$$ct = (r + l) - d \tag{1.1}$$

compared to the direct light from the source event.

Let us now assume that the source event is sufficiently far away from Earth such that $\gamma \sim 0$, and $l = d - z$; a reasonable assumption given that the the closest LEs discovered in the Milky Way (MW) have $\gamma \leq 8^{o}$ or 0.14 radians (Rest et al., 2011). Then Equation 1.1 becomes

$$r = z + ct \tag{1.2}$$

Squaring both sides, and substituting in

$$r = \sqrt{\rho^2 + z^2}$$

yields:

$$\rho^2 = 2zct + (ct)^2 \tag{1.3}$$

Here, z is distance along the line of sight, and ρ is a projected distance in the plane of the sky. Equation 1.3 is called the Light Echo equation, and describes a parabolic surface symmetric about the z-axis with its focus at the source. By knowing the delay time, t, and the separation between the source and LE, ρ, we can make predictions about the viewing angle of the LE, θ.

The observation of a LE is highly dependent on favourable placement of scattering material, most commonly dust clouds or sheets, and the distribution of the scattering dust plays a major role in the structure and temporal evolution of the LE.

1.2.2 Observations of Light Echoes

Since LEs were first formally understood in 1939, they have proved powerful methods for late-time study of transient events. The scattered light preserves both the spectral energy distribution (SED), and the light curve of the initial SN. These can be used for posthumous classification of ancient SNe for which no modern observations are present; as was demonstrated in the cases of both Tycho Brahe's 1572 SN (hereafter Tycho), and the Cassiopeia A SN (hereafter Cas A) which were identified as Type Ia (Krause et al., 2008b, Rest et al., 2008), and Type IIb (Krause et al., 2008a, Fabian, 2008) respectively through observations of their LEs.

Systems also exist in the MW and Large Magellanic Cloud (LMC) for which multiple LE systems have been discovered. By the formalism laid out in the previous section, each individual LE represents a unique viewing angle, θ, or a unique line of sight to the source event, allowing for true three-dimensional imaging - the only area in astronomy in which this is possible. This has been used to great effect in directly confirming asymmetry in the Cas A, and SN 1987A outbursts, an example of which is shown in Figure 1.2 (Rest et al., 2011, Sinnott et al., 2013).

SN 1987A has been one of the most widely studied astronomical events in history. It had the brightest apparent magnitude of any known SN since Kepler's SN in 1604, despite being located at 50 Kpc (Blanco et al., 1987). It was also the first SN to be extensively studied with modern instrumentation (Blanco et al., 1987). The SN itself was remarkable for a number of reasons, including being the first event for which the progenitor star was identified beforehand (Arnett et al., 1989), as well as the first detected source of extra-solar neutrinos (Hirata et al., 1987, Bionta et al., 1991). The Hubble Space Telescope also revealed concentric rings in the circumstellar material (CSM) (Luo & McCray, 1991). Faint LE complexes were identified from SN 1987A and are well known in the literature (Crotts et al., 1989, Wampler et al., 1990, Crotts & Kunkel, 1991, Rest et al., 2005).

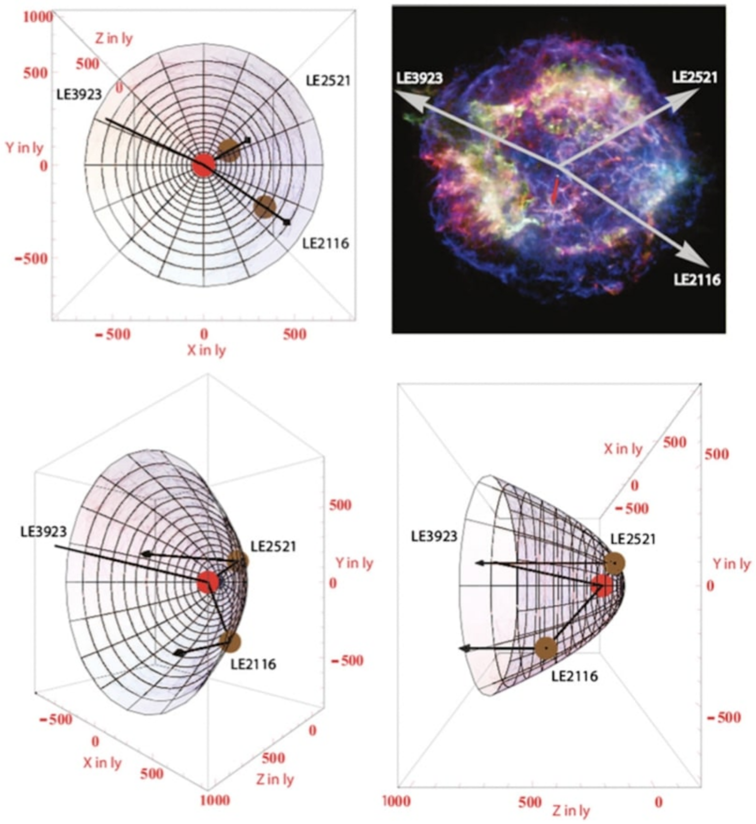

FIGURE 1.2: Schematic example of how multiple LEs can be used as individual lines of sight to view a SN. Figure from Rest et al. (2011).

Extraction of the SN SED and light curve from the scattered light is a non-trivial process and is complicated by both the geometry of the dust, and additional effects of atmospheric seeing. Dust generally has a non-zero thickness, and therefore a range of epochs of light can be present in one LE. The inclination of the dust can also act to compress or stretch the SED (Krause et al., 2008a). These effects however, are not the subject of this work, and will not be discussed further.

If the geometry of the dust is known, as well as its scattering efficiency and dust grain cross-section; the surface brightness flux of a LE can be predicted (e.g. Dwek, 1983, Schaefer, 1987, Sparks, 1994). From Sugerman (2003); if the scattering efficiency, $S(\lambda, \cos\theta)$, is known, as well as the thickness of the LE along the line of sight, Δz, and in the plane of the sky, $\Delta\rho$, the surface brightness flux of the LE is found to be

$$f_{SB}(\lambda, t, \phi) = F(\lambda) n_H \frac{c\Delta z}{4\pi\rho\Delta\rho} S(\lambda, \cos\theta) \tag{1.4}$$

where $F(\lambda)$ is the integrated flux from the source event, and n_H the number density of Hydrogen.

Scattered LEs are much fainter than the original SN - compare a peak apparent magnitude of +2.9 for SN 1987A, to its brightest LEs at 19.3 mag/arcsec^2 (West et al., 1987, Xu et al., 1994, Sinnott et al., 2013). Moreover, Patat (2005) calculated that for Type Ia SNe, LEs will generally occur ∼10 mag fainter than the peak SN brightness. It is however, rare that dust is well characterized a priori, even for fields in the MW, which makes predicting LE brightness a difficult task. In practice, it is more common to use observed LEs to infer dust properties.

Compounding this with the uncertainties in position of potential scattering dust makes LEs notoriously difficult to detect. These difficulties are aptly summed up in the attempts of Oaster (2008) to build a survey strategy for LEs from historical SNe in the MW, namely Cas A, and Tycho. Using the 4 m Mayall Telescope on the Kitt Peak National Observatory (Dey & Valdes, 2014); a search was conducted for LEs, with telescope pointings based on a probability model. Using MW dust maps from Arenou et al. (1992) the model took into account effects of absorption, distance, and scattering direction to predict potential positions of the brightest LEs. This model was compared with a pre-existing IRIS survey strategy (reprocessed IRAS data; Miville-Deschênes & Lagache, 2005). Although the IRIS fields proved marginally more fruitful, with a 5% detection rate, it was concluded that the model fields failed to detect more LEs than would be expected by chance - said another way; *the survey did not perform better than a strategy of random fields.* It is worth noting that IRIS is an infrared cirrus dust mapping survey, and not a specialized LE observing strategy. Furthermore, of the 12 LEs discovered, four of them were present in what were deemed to be 'low probability regions' by the Oaster model.

Later work by McDonald (2012) searching for LEs associated with SN 1054 and SN 1181 encountered similar difficulties. 367 Sloan g′ and 195 Sloan r′ fields around the SNe were imaged twice, however no LE candidates were discovered brighter than the survey limit of 24.0 mag/arcsec^2. The author concluded that *a survey strategy has yet to be discovered which is superior to random pointings.*

These works highlight the difficulties in large scale LE surveys in fields of the MW and nearby galaxies. The likelihood of detecting a LE is confounded by large uncertainties in dust distribution, age, and distance. When considering LEs specifically from Type II SNe there are additional difficulties stemming from wide ranges in outburst luminosities, as well as generally lower peak brightnesses when compared to SNe of Type Ia (Young & Branch, 1989, Phillips, 1993). It is no surprise then, that LEs from Type II SNe are underrepresented in current MW and Magellanic Cloud surveys, and considering the relative rarity of SNe, one per 50 years in the average galaxy and no naked-eye SNe since 1604 in the MW, this field has yet to reach its full potential (Cappellaro et al., 1999, Diehl et al., 2006). An object containing multiple Type II SNe with known ages has the potential to provide a firmer basis for our statistics of LE detectability.

1.3 NGC 6946

The nearby, face-on spiral galaxy NGC 6946, colloquially known as the "Fireworks Galaxy", is such an object. Located at a distance of 7.72 Mpc in the constellation Cepheus, it has a mean surface brightness of 23.5 mag/arcsec^2 in the V band (Kim & Chun, 1984, Anand et al., 2018). Remarkably, NGC 6946 has had *ten* SNe discovered in it during the past 100 years - the first recorded in 1917 and the most recent in 2017. The galaxy therefore could contain a set of potentially detectable LEs from SN events at various stages of decay (Sugerman et al., 2012). It is the ideal object in which to undertake a study of the detectability of LEs from Type II SNe. The locations of the ten SNe within the galaxy are shown in Figure 1.3.

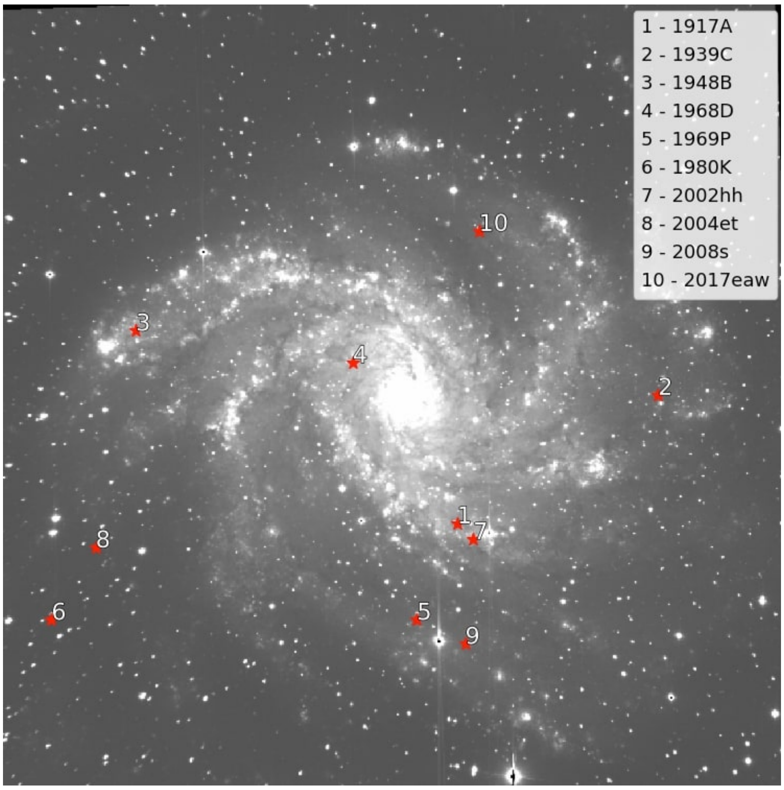

FIGURE 1.3: Locations of the ten SNe within NGC 6946. The red stars represent the location of each SN. The background image is the deep frame from our SITELLE observations (see Chapter 2.3).

1.3.1 A History of Supernovae in NGC 6946

The ten SNe in NGC 6946 are relatively evenly dispersed over the 100-year period beginning in 1917. The events in the later part of the 20^{th} and early 21^{st} century are well classified and have many observational followups of the initial discovery across multiple wavebands. However, many of the earliest SNe have evaded proper classification due to a lack of data. The main astrometric data for the SNe are summarized in Table 1.2, and photometric and spectroscopic properties in Table 1.3.

The ten SNe span a wide range of peak apparent magnitudes, and cover most sub-classes of Type II SNe; although, with the exception of SN 1948B, all SNe prior to 1980

Table 1.2: Summary of the major astrometric properties of the ten SNe in NGC 6946. J2000 positions and offsets are from SIMBAD and the Asiago Supernova Catalogue and references therein (Wenger et al., 2000, Barbon et al., 1999). Wherever possible, radio detections were used to confirm positions and offsets.

Designation	Discovery Date	RA	Dec	Offset
1917A	19 July, 1917	20:34:46.9	+60:07:29	37"W, 105"S
1939C	17 July, 1939	20:34:24.06	+60:09:29.9	215"W, 24"N
1948B	06 July, 1948	20:35:21.5	+60:10:16	222"E, 60"N
1968D	29 February, 1968	20:34:58.40	+60:09:34.4	45.3"E, 19.8"N
1969P	11 December, 1969	20:34:51.3	+60:06:14	5"W, 180"S
1980K	28 October, 1980	20:35:30.13	+60:06:23.51	280"E, 166"S
2002hh	31 October, 2002	20:34:44.29	+60:07:19.0	60.9"W, 114.1"S
2004et	27 September, 2004	20:35:25.33	+60:07:17.7	247.1"E, 115.4"S
2008S	01 February, 2008	20:34:45.33	+60:05:58.4	53"W, 196"S
2017eaw	14 May, 2017	20:34:44.238	+60:11:36.00	61.0"W, 143.0"N

lacked the sufficient photometric and spectroscopic followup required for direct classification. LEs from any of these SNe would provide the requisite spectra for sub-classification. SN 1969P is particularly noteworthy in that there was no optical followup whatsoever on the SN discovery until almost a year later (Rosino, 1971). Multiple followups across many wavebands ensure the accuracy of the positions of SNe from the 21st century. SNe 1968D, and 1980K have positions confirmed through radio detections as well as in X-Ray wavelengths (Schlegel, 1994, Hyman et al., 1995).

There is some debate surrounding the validity of the classification of SN 2008S as a Type IIn. The initial classification is by Stanishev et al. (2008), based on narrow Hα and Hβ lines found in a low resolution spectrum taken by the Nordic Optical Telescope. Later work by Botticella et al. (2009) claims that SN 2008S is a rare electron capture SN from an asymptotic giant branch (AGB) progenitor, based on a lack of spectral evolution in the SED. Further work suggests that 2008S is a so-called SN imposter; a periodic eruption of a luminous blue variable (LBV) star, driven by super-Eddington winds (Smith et al., 2009). Similar mechanisms are believed to have driven the Great Eruption of η-Carinae (Davidson & Humphreys, 1997, Rest et al., 2012). No progenitor

TABLE 1.3: Summary of major photometric and spectroscopic properties of the ten SNe in NGC 6946. SN classifications are from the Asiago Supernova Catalogue and references therein (Barbon et al., 1999). Discovery magnitudes are from the Transient Name Server.

Designation	Type	Discovery Apparent Magnitude
1917A	II*	+14.6 [1]
1939C	I*	+13.1 [1]
1948B	IIP	+15.1 [1]
1968D	II*	+13.5 [1]
1969P	-*	+13.9 [1]
1980K	IIL	+13.0 [1]
2002hh	IIP	+16.5 [2]
2004et	IIP	+12.8 [2]
2008S	IIn/LBV?	+17.6 [2]
2017eaw	IIP	+12.8 [2]

* insufficient followup for proper classification.
[1] Discovery magnitude via photographic plates.
[2] Discovery magnitude via CCD.

object has been identified at the 3σ level in V, R, or I bands, however archival Spitzer 5.8 and 8.0 µm data reveals a $\sim$10 $M_\odot$ source coincident with the position of SN 2008S (Welch et al., 2008, Prieto et al., 2008, Wesson et al., 2010). If this is indeed the stellar progenitor of the 2008S event, it is extremely unlikely that SN 2008S was an LBV eruption, as LBVs are exclusively supergiant stars (Humphreys, 1978).

1.3.2 Light Echoes in NGC 6946

NGC 6946 has long been identified as potentially housing multiple LE systems. Early work by Boffi et al. (1999) aimed to identify LE candidates based on the optical colours of patches of emission near known SNe. All SNe prior to 2002hh in NGC 6946 were part of their sample, however none of the emission patches they identified yielded promising LE candidates.

Of greater consequence are the recent discoveries of LEs from both SN 2002hh and 2004et.

SN 2004et

Observations of the mid-infrared (MIR) continuum from SN 2004et strongly suggest the presence of dust along the line-of-sight (Sahu et al., 2006, Misra et al., 2007). Studying the evolution of the SED over time, Kotak et al. (2009) found that the late-time SED is best fit with a three-component model: hot emission from optically-thick gas, warm emission from radiatively-heated dust in the ejecta, and a cold component due to an MIR LE in the interstellar-medium (ISM) dust. SED fitting at 464 days after outburst gives a LE with peak brightness of 1.2×10^{-26} erg/s/cm^2 at 50 µm. There has been no published followup to confirm this. Moreover, MIR LEs do not preserve the spectrum of the original incident light since they are dominantly the result of re-radiation due to heated dust grains. Despite these differences compared to scattered optical LEs, MIR re-radiation is still considered to be a LE in the literature.

SN 2002hh

SN 2002hh was directly observed to be surrounded by a massive dust cloud in followup Spitzer IRAC observations, in all four of its wavebands, during the epoch from 590-994 days after outburst (Barlow et al., 2005, Meikle et al., 2006). Like SN 2004et, SED fitting indicated the presence of a MIR LE from the SN. Late-time photometry and spectroscopy by Welch et al. (2007) with Gemini/GMOS-N, followed the evolution of the SN from 661 to 1358 days after outburst. No significant fading of the Hα flux, nor of flux in the R or I bands, confirmed the presence of an extremely bright LE with an Hα flux of 4×10^{-13} erg/s/cm^2/arcsec^2. Eleven years after outburst, the Hα flux of the LE was reported by Andrews et al. (2015) to have dropped to 3×10^{-17} erg/s/cm^2/arcsec^2.

To have the greatest opportunity of recovering either of these LE complexes, as well as potential others from the remaining eight SNe, an observational program needed to be designed which would probe deep into spectra of objects in the vicinity of NGC 6946 SNe.

Chapter 2

Observations

2.1 Observational Characteristics of Light Echoes

There are two common methods of conducting LE surveys: difference imaging (photometry), and spectroscopy. Difference imaging surveys, like McDonald (2012), use techniques to attempt to resolve the apparent motion of a LE over scattering dust; the geometry of which is demonstrated in Figure 2.1.

The typical apparent motion of a LE in the MW is of the order a few tens of arcseconds per year (Sinnott, 2013). To detect this apparent motion, difference imaging surveys require multiple, high-spatial resolution images of the same field, separated in time by weeks or months. Difference imaging can be tedious, as human eyes still outperform computers in finding faint changes in brightness between two images (McDonald, 2012).

Spectroscopy (e.g. Welch et al., 2007, Andrews et al., 2015) can provide more definitive evidence for LEs, and is often used as a followup for LE candidates determined by difference imaging. MIR spectroscopy (e.g. Welch et al., 2007, Kotak et al., 2009) uses SED fitting to attribute excesses of IR emission to the presence of LEs, as discussed in Section 1.3.2. Optical spectroscopy, which will be the subject of the remainder of this thesis, can be used to directly observe the defining spectral signatures of SNe within LEs - the P-Cygni Hα line profile.

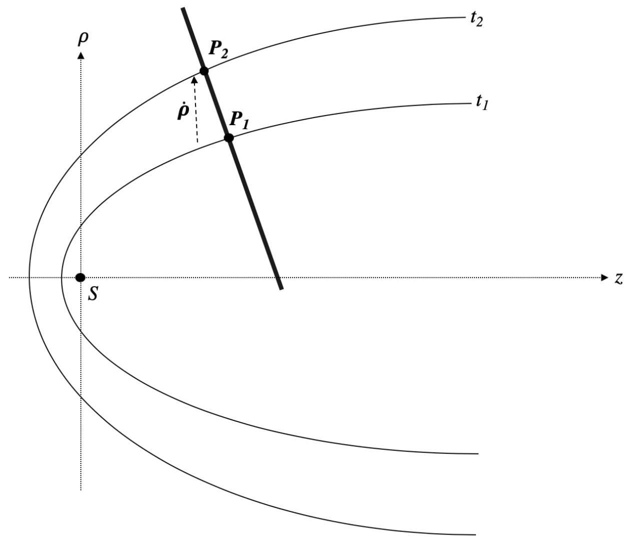

FIGURE 2.1: The geometry demonstrating the apparent motion of a LE from source event S, across a dust sheet. As time increases from t_1 to t_2, so too does the size of the iso-time ellipse. Where the ellipse intersects the dust sheet, we see a LE. At time t_1, the LE appears at P_1, but appears to move to P_2 at later time t_2. We therefore observe a projected apparent motion, $\dot{\rho}$, of the LE across the dust sheet.

2.1.1 The P-Cygni Line Profile

The characteristic spectral feature of core-collapse SNe and their LEs is the Hα P-Cygni line profile. As illustrated in Figure 2.2, the peculiar P-Cygni line profile (named after the first star in which this spectral profile was observed) is caused by an expanding shell of material around a star. It is a combination of a red-shifted emission, and blue-shifted absorption feature (De Groot, 1969, Beals, 1953).

Such an expanding shell is believed to exist in any stellar system which has experienced extreme mass loss (Beals, 1932, Struve, 1935). Although the seminal work on this topic was in the context of novae and Wolf-Rayet stars, it is clear that the material thrown off by the star during a SN, satisfies the criteria to create a P-Cygni profile (Kirshner et al., 1973). In practice, the Hα P-Cygni lines produced in SNe are quite long-lived, persisting for years after the eruption. Furthermore, ejecta from SNe travel at velocities $\sim 5 \times 10^3$ km/s, causing the spectral lines to be broadened by 5 nm or more

(Hamuy & Pinto, 2002).

The goal of optical spectroscopy is to observe and fit faint Hα P-Cygni lines for unequivocal detections of SN LEs. Since they are the defining features of core-collapse SNe, the continued presence of a P-Cygni profile in the Hα line, many years after maximum light, will be treated as our LE detection criteria throughout the rest of this study.

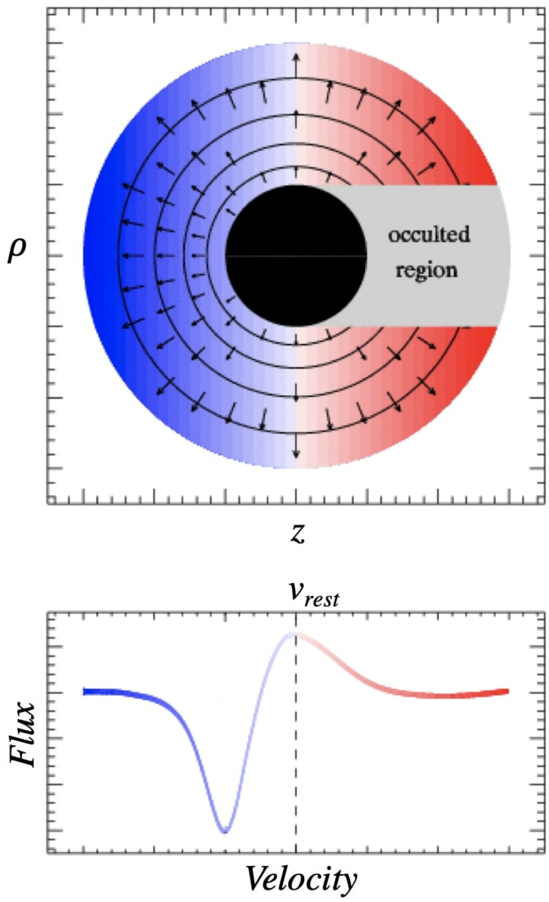

FIGURE 2.2: The expanding shell of mass, thrown off by the star during the SN leads to the formation of a P-Cygni line profile. Red-shifted emission is due to the material behind the star, expanding away from the observer. The blue-shifted absorption is due to the material in front of the star, expanding towards the observer. The line is centred on the star's rest frame velocity. Image adapted from Blondin (2018).

2.2 SITELLE: an Imaging Fourier Transform Spectrometer

All previous LE search strategies share a common difficulty - the selection of fields to maximize the probability of a successful detection; which was the topic of Section 1.2.2. Previous spectroscopic studies in particular are limited by their use of slit spectroscopy (e.g. Gemini/GMOS). Searching for LEs with spectroscopy has long been an unfavourable method, as for nearby galaxies, a slit would need to be positioned directly on a LE to observe the characteristic P-Cygni line profile. This is an extremely improbable occurrence in blind survey studies, hence why spectroscopy is usually only performed once LE candidates have been located through difference imaging. However, even when the position of a LE is known, distortion of the LE profile can occur if the LE is improperly centered in the slit (Rest et al., 2011, Sinnott et al., 2013). In more distant galaxies, a slit could potentially contain all of the emission from a LE - especially for decades old SNe. However, even in these cases, slit spectroscopy likely includes too much contamination from stellar emission to disentangle a faint LE signal.

The advent of integral field unit (IFU) spectroscopy has the potential to revolutionize the manner in which LE searches are conducted. Instead of having to haphazardly position a slit over the region of interest, IFU data provides spatially-resolved spectroscopy.

SITELLE (Spectromètre Imageur à Transformée de Fourier pour l'Etude en Long et en Large de raies d'Emission) is an optical imaging Fourier transform spectrometer (IFTS) on the Canada-France-Hawaii Telescope (CFHT). This instrument saw "first light" in July 2015 (Drissen et al., 2010). Unlike other IFUs like the Sloan Digital Sky Survey MaNGA (Mapping Nearby Galaxies at APO) survey, which use fibre bundles (e.g. Drory et al., 2015), an IFTS uses interferometry to achieve spatially resolved spectral data.

The core mechanism behind SITELLE is a Michelson Interferometer (e.g. Figure 2.3). As one of two the mirrors in a Michelson Interferometer is moved through a set distance, it introduces a range of optical path differences (OPD) between the beam reflected, and the beam transmitted by the beamsplitter. These OPDs produce different final intensities at the detector once the beams have recombined. For example: if there is no OPD, the two beams are perfectly in phase and the intensity at the detector is a maximum. However, if the OPD is equal to exactly one-half of the wavelength of the incident beam, the two beams are perfectly out of phase, and produce zero intensity at the detector. By sampling a range in OPDs an interferogram is produced; mapping the intensity at the detector as a function of OPD.

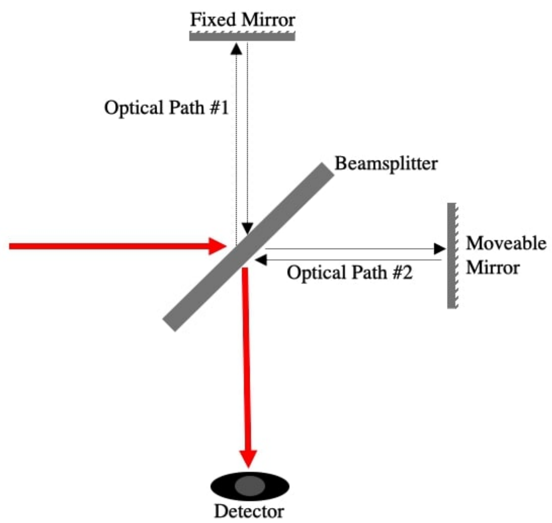

FIGURE 2.3: A schematic of a basic Michelson interferometer. Light enters the apparatus and is incident on the beamsplitter which is coated in such a way that half of the light is transmitted, and half is reflected. The reflected and transmitted beams are each reflected by another mirror, and are recombined by the beamsplitter. The result of the interference between the two beams is received by the detector. One of the two mirrors is movable, such that the optical path length travelled by one of the beams can be altered.

In a simple Michelson Interferometer, some of the incident light is always reflected back to the source and is lost for the purposes of observation. The interferometer implemented in SITELLE was designed with its components aligned off of the optical axis (e.g. Figure 2.4) in order to include a second detector. The two detectors ensure that all light incident on the instrument is available to be analyzed. The maximum OPD achieved sets the spectral resolution of the observation. However, the interferogram must be properly Nyquist sampled to obtain the required resolution; one cannot just immediately move from zero, to an arbitrarily large OPD. This means the mirror step size, the incremental amount by which the mirror is displaced, should be roughly half of the shortest wavelength in the resulting spectrum (Drissen, 2016).

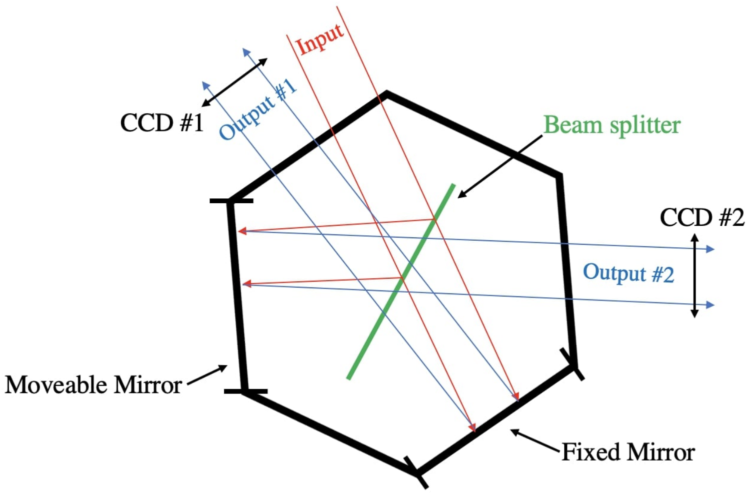

FIGURE 2.4: A schematic of the more complicated, off-axis setup of SITELLE's interferometer. The two detectors ensure that all of the light incident on the instrument is collected and analyzed.

Each of SITELLE's two detectors records an individual interferogram, which are then co-added to produce an overall interferogram for the observation. For a perfectly monochromatic incident beam, the interferogram is a sine wave. Astronomical sources though are rarely so well behaved, and the final interferogram is a combination of various sinusoidal waveforms. Fourier analysis is required to convert the acquired interferogram into spectral data.

Using Fourier's equation:

$$\mathcal{F}(\omega) = \frac{1}{\sqrt{2\pi}} \int_{-\infty}^{\infty} f(t) e^{-i\omega t} dt \tag{2.1}$$

The interferogram, $f(t)$, is decomposed into its spectrum in frequency space, $\mathcal{F}(\omega)$. For a perfectly monochromatic source, this produces one single spectral line at the frequency of the incident light. For a composite light source, the Fourier decomposition produces a series of spectral lines, as demonstrated in Figure 2.5. In practice, an infinite OPD cannot be reached in order to produce a perfect sine wave in the interferogram. The spectral line shapes produced by SITELLE (or any IFTS) is a sine cardinal, or 'sinc', instead of a delta function. This results from the Fourier transform of a sine wave convolved with a rectangular boxcar - to reflect the finite nature of the interferogram.

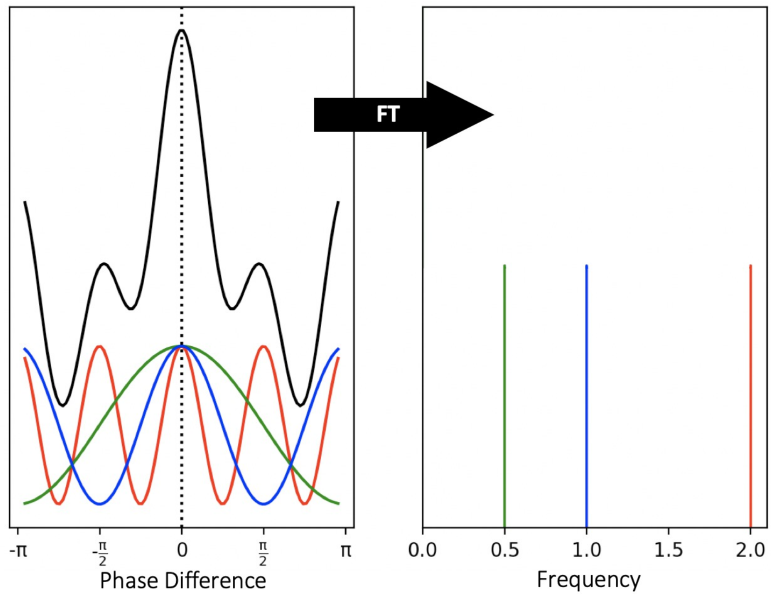

FIGURE 2.5: An example of the Fourier spectral decomposition of a composite incident beam. On the left, the interferogram for the incident light (black) is a combination of three monochromatic waves (blue, green, red). On the right side, the result of the Fourier decomposition yields three spectral lines, corresponding to the frequencies of each of the component waves.

Each pixel records its own interferogram, and the resulting data product is a cube, with complete spectral information for every pixel in the two-dimensional image. At the time of its commissioning, SITELLE had the largest field of view (FOV) of any optical IFU at $11' \times 11'$. It has a pixel scale of $0.32''$, and is capable of reaching R$\sim 10^4$ of spectral resolution. SITELLE has six built-in filters covering optical wavebands from

350 to 900 nm. The filters are necessary, due to SITELLE's method of operation, to prevent aliasing within the spectra - further explanation of which will be provided in Chapter 3.2.1.

With its high spectral resolution and small pixel scale, SITELLE's primary scientific purpose is spatially-resolved spectroscopy of extragalactic emission line regions (Martin et al., 2017, Rousseau-Nepton et al., 2018). However, SITELLE also possesses attributes which make it a useful instrument for a somewhat 'off-label' SN LE search. As shown in Figure 2.6, the FOV is perfectly matched to the size of NGC 6946 and the positions of all ten SNe can be captured within a single pointing. The IFU capabilities also mean that spectral information is gained for over 4-million pixels across the entire frame. Observing NGC 6946 with SITELLE is an efficient and near-optimal strategy to search for LEs in the most productive galaxy known for SNe.

2.3 Our Observational Program

We designed an observing program for the 2018B semester (proposal, and observation ID 18BC17) to use SITELLE to search for LEs from any of the ten post-1917 SNe, as well as from any historical SNe for which there are no recorded observations.

Due to the extreme Doppler broadening of the Hα P-Cygni line profiles, a resolution of only R = 300 would be sufficient for a detection in the dedicated Hα filter, SN3 (651-685 nm). As shown in Figure 2.7, an Hα P-Cygni line profile broadened by a few thousand kilometres per second would completely fill the SN3 filter bandpass. We therefore did not need to use the full spectral resolution capabilities of SITELLE, and decided to sacrifice spectral resolution in order to obtain a very deep image, and potentially detect signatures of the faintest possible LEs.

This trade-off in spectral resolution for image depth was a key difference of our use of this instrument. Most of the scientific work done with SITELLE uses a few hundred interferometer steps, and short (tens of seconds) exposures per step. We proposed 12

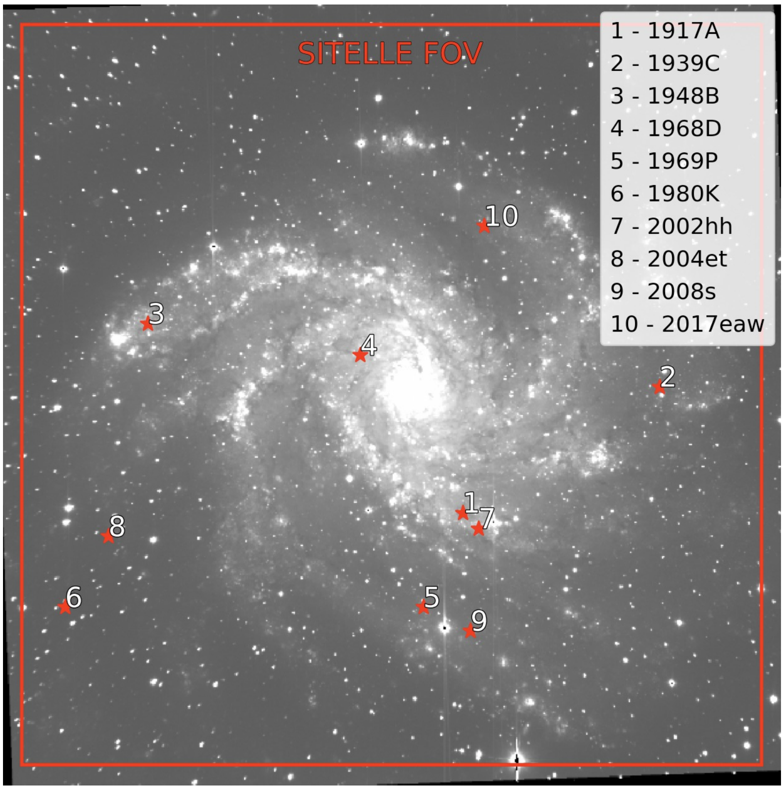

FIGURE 2.6: NGC 6946 fits perfectly in the $11' \times 11'$ FOV of SITELLE. The locations of all ten SNe can be captured in a single pointing. As in Figure 1.3, the red stars represent the locations of the ten SNe.

hours of observations with only 51 interferometer steps, but an exposure time of 279 seconds per step. This would allow us to detect our target broadened Hα lines at a flux of 5×10^{-16} erg/s/cm^2/arcsec^2 with a total signal-to-noise ratio (S/N) of five. This flux corresponds to almost five magnitudes below the peak brightness of SN 2004et. We also expected to detect the previously-discovered LE from SN 2002hh with significant S/N.

All 12 requested hours were allocated to us by the time allocation committee. The observations were broken up into three, four-hour observing blocks to be completed in QSO (Queued Service Observation) mode starting October 3, 2018. Three observing blocks were necessary to accommodate the $+60^{\circ}$ declination of the galaxy, resulting in it being below an airmass of 1.5 for only about four hours per night as seen from Mauna Kea. Unfortunately, uncooperative weather resulted in only one of the three

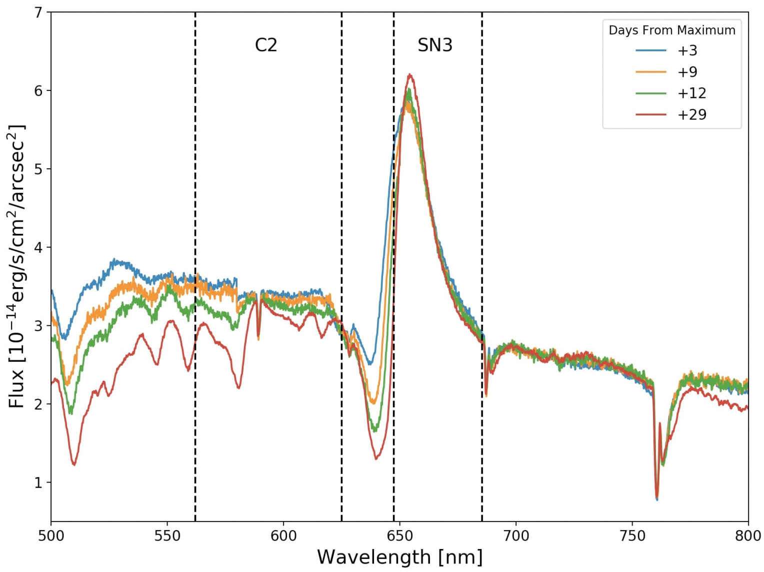

FIGURE 2.7: Four spectra from SN 2004et spanning a month after initial outburst (Sahu et al., 2006). The Hα lines display the characteristic P-Cygni profile and have been broadened by ~40 nm to completely fill the SN3 filter bandpass. The bandpass of the SN3 filter, as well as the neighbouring C2 filter are denoted with dashed black lines.

observing blocks being completed, and we only acquired four hours of data. The loss of observing time increased the limiting surface brightness of the survey by approximately 0.6 mag/arcsec^2; from 24.9 mag/arcsec^2 in the R-Band with the full 12 hours of data, to 24.3 mag/arcsec^2.

The standard data reductions were completed on site with the ORBS[1] (Outil de Réduction Binoculaire pour SITELLE) software package, version 3.4 (Martin et al., 2015). These include standard astronomical reductions such as bias, dark frame, and flat field corrections, as well as cosmic ray removal. In addition there are reductions specifically required to process IFTS data. ORBS completes the combination and alignment of the two interferograms, using background standard stars for reference, and also includes a phase correction to take into account the off-axis configuration of SITELLE's optical elements. Lastly, ORBS enables flux and wavelength calibrations, meaning no further

[1]https://github.com/thomasorb/orbs

data reductions are required once the datacube has been received.

Losing two-thirds of the observing time we were granted significantly impacts the brightness of LEs that we could potentially uncover, as demonstrated by the 0.6 mag/arcsec^2 increase in limiting surface brightness. As such, we required that extra emphasis be placed on developing a LE search methodology which made the most of the data that we did receive. The calibrated datacube can be retrieved from the CADC with product ID 2307000p.

Chapter 3

Data Analysis

This chapter outlines the various analyses that were performed on the SITELLE datacube after the completion of the initial data reductions.

3.1 Motivation for Continuum Fitting

The primary goal of optical LE spectroscopy is to detect and fit the characteristic Hα P-Cygni profiles indicative of the presence of a SN LE. As can be seen in Figure 2.7 though, SITELLE does not have a filter that completely encompasses an Hα line broadened by the velocities expected in a SN. The SN3 filter captures the 656 nm rest frame wavelength of the Hα line, but due to the filter's 34 nm bandwidth, broadening by $\gtrsim$5000 km/s will cause the line to completely fill the bandpass. As the SN3 bandpass covers the range of 651 - 685 nm, it captures only the red-shifted emission component of the P-Cygni profile.

Unfortunately, the blue-shifted absorption component falls between the SN3 and neighbouring C2 filter (562 - 625 nm), meaning we can only observe the emission component of a P-Cygni profile. This situation is less than ideal since it prevents us from searching our spectra for full P-Cygni line shapes. It would be possible to purchase a custom filter for SITELLE specifically for this program, but time and cost prevented us from exercising this option.

3.1.1 ORB and ORCS

ORCS (Outils de Réduction de Cubes Spectraux), and its backend ORB, is the data processing software package, written in python, and designed specifically to handle SITELLE data (Martin et al., 2015). It is publicly available to download [1]. ORCS handles the extraction of spectra from the datacube, as well as the mechanisms for fitting high spectral resolution emission lines. The fitting procedure is highly customizable by the individual user, allowing choice between a Bayesian or classical fitting algorithm, specification of line velocities, subtraction and correction of sky lines, etc. (e.g. Martin et al., 2016).

ORCS functions optimally on high spectral resolution data, where there is clear distinction between neighbouring spectral lines. Large uncertainties are introduced when fitting low resolution data, as is demonstrated with a higher resolution, archival SITELLE datacube of NGC 6946[2]. Our observations span the SN3 filter with 49 IFTS steps, which in wavelength space corresponds to $\sim$2.15 nm/step at the wavelength of Hα. We have an exposure time of 93 s/step. The archival cube, observed starting July 3, 2017, is much higher spectral resolution at $\sim$0.3 nm/step, but the exposure time is only 36.1 s/step, for a total integration time of three hours. These observations have a limiting surface brightness of 21.9 mag/arcsec^2 in the R-Band.

The differences in resolution between the two cubes is shown in Figure 3.1. It can be clearly seen that although the five distinct emission lines (Hα, [NII]654.8, 658.4, and [SII]671.7, 673.1) are well-resolved in the archival cube, the individual lines are not resolved in our data. This was expected, since the emission lines will be well sampled at 0.3 nm/step in the archival data, whereas only two frames encompass the wavelengths of both [NII] lines and Hα in our data.

It is clear how this would introduce difficulties when attempting to fit emission lines with ORCS. In the archival cube, it is obvious which line is Hα versus, [NII]654.8, or

[1] https://github.com/thomasorb

[2] CADC product ID 2141443p

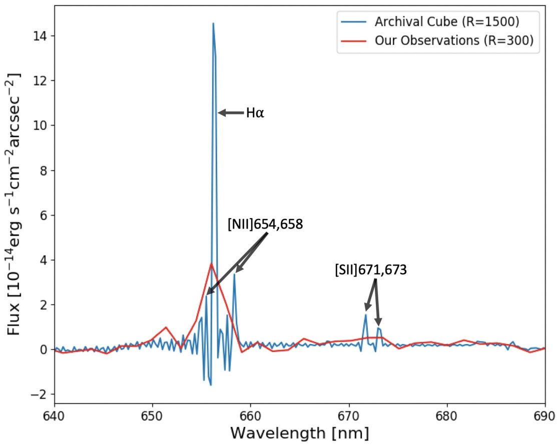

FIGURE 3.1: A comparison between high and low resolution SITELLE spectra. Both spectra are of the same HII region in NGC 6946 and show the common emission lines: Hα, [NII]654.8, 658.4, and [SII]671.7, 673.1. These individual lines are resolved in the archival cube, however in our data, the SII doublet as well as the complex containing Hα and the NII doublet are unresolved.

[NII]658.4, etc. However, there is a degeneracy in our data when trying to fit these same three lines. This is where ORCS Bayesian fitting routines are intended to be most useful. The Bayesian algorithm requires some knowledge, or at least a best estimate, of the line velocities in order to attempt to break the degeneracies occurring in low resolution data.

To test how accurate ORCS was in extracting spectral line fluxes and velocities from low resolution data, fit results of the same region were compared between our observations, and the archival cube. In addition, velocity data from the ORCS fits of the archival cube could be reused as input for the Bayesian fitting of our data. The results of these two fits are summarized in Table 3.1 and visualized in Figure 3.2.

Although it appears that ORCS has fit the low-resolution spectrum quite well, the fitting results in Table 3.1 clearly show how much ORCS struggled with breaking the fitting degeneracies. The values from the high resolution fit were used as priors in ORCS's Bayesian fitting algorithm, and the resulting line parameters are vastly different from what one would expect. There is no reason to expect that the velocity or broadening of the individual lines should vary wildly between the two datacubes, especially in spectra

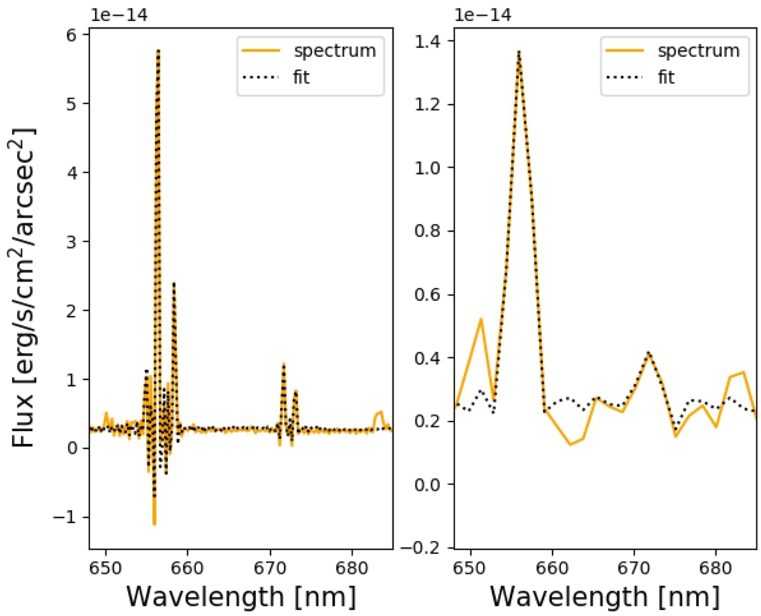

FIGURE 3.2: A comparison of ORCS fit results from a spectrum in our data (right), and in the archival cube (left). Each individual line is fit nicely in the high resolution data. In our data, the general line complexes have been captured, but ORCS has been unable to break the large degeneracies in the parameters for individual lines making up the broad shapes.

of the same region. Differences in flux can perhaps be partially attributed to different exposure times between the two sets of observations. The presence of NaN values as errors for all low-resolution parameters, as well as some clearly incorrect negative fluxes, indicate that ORCS was not able to accurately fit our low resolution data, even with its Bayesian algorithm.

In addition to difficulties with low resolution data, ORCS can also struggle with fitting spectra where the continuum deviates significantly from a constant value (e.g. Figure 3.3). ORCS tends to impose a flat continuum on the spectrum, which not only incorrectly describes the continuum itself, but also introduces either over, or under-estimations of fluxes in emission lines. As will be discussed in Section 3.2, accurate characterization of the continuum is of critical importance to our study. ORCS was designed primarily to fit emission lines, whereas understanding the continuum is a core concern of our work.

TABLE 3.1: Results of ORCS fits of high and low resolution spectra.

Line	High-Resolution			Low-Resolution		
	Flux (erg/s/cm^2)	Broadening (nm)	Velocity (km/s)	Flux (erg/s/cm^2)	Broadening (nm)	Velocity (km/s)
[NII]6548	2.7(2)e-14	2.66(.21)	27.1(7)	4.0e-14	46.5	36.5
Hα	2.1(3)e-13	2.66(.21)	27.1(7)	3.0e-13	46.5	36.5
[NII]6583	6.6(2)e-14	2.66(.21)	27.1(7)	-6.7e-15	46.5	36.5
[SII]6716	3.0(2)e-14	2.66(.21)	25.7(4.0)	6.7e-14	46.5	313.7
[SII]6731	2.0(2)e-14	2.66(.21)	25.7(4.0)	-3.6e-14	46.5	313.7

Values in brackets are the error in the final decimal places, associated with each quantity. For the low-resolution data, errors were all 'NaN' values.

These issues made it clear to us that relying solely on ORCS would not be the ideal manner in which to move forward with our study. When required, ORB version 3.4, and ORCS version 2.4 were used in parts this work

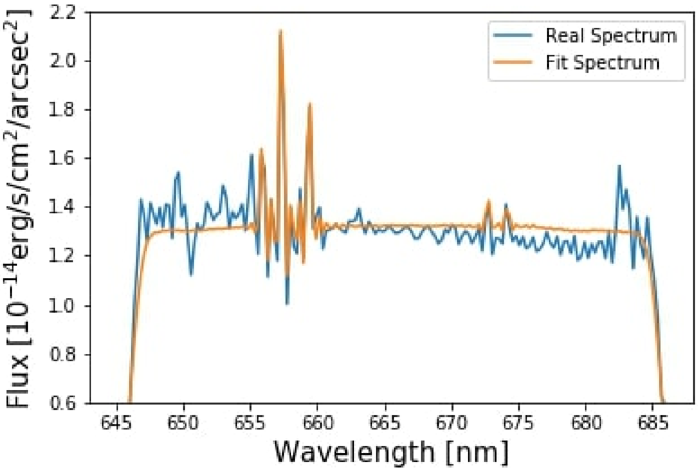

FIGURE 3.3: An ORCS fit of a high-flux continuum region near the galactic centre in an archival SITELLE datacube of NGC 628. Note how ORCS has fit the emission lines, but has failed to accurately capture the slope of the continuum.

3.2 A Statistical Methodology for Continuum Fitting

As shown in Figure 2.7, the emission component of the Hα P-Cygni line profile completely fills the SN3 bandpass for velocities characteristic of SN eruptions. Furthermore, due to the position of the rest frame Hα line near the blue edge of the filter, it is predominately the negatively-sloped component of the emission that is seen in the SN3 filter. A highly broadened P-Cygni profile in the Hα line would therefore look just like negatively-sloped continuum in our data. Without the tell-tale absorption component, or even the positively-sloped side of the emission line, a novel method was required to distinguish our broadened P-Cygni Hα lines from the regular galactic continuum.

Two factors were key in our considerations of the structure of the galactic continuum: the dominant stellar populations in NGC 6946, as well as the width of the SN3 filter. As can be seen in Figure 3.4, for all but the hottest stars, the peak of the SED is situated in, or near to the wavelength range corresponding to the SN3 filter bandpass. A, B, and O Typed stars, with temperatures $7000K < T < 50000K$, would impart large negative slopes onto the continuum within the SN3 filter (Habets & Heintze, 1981). However, these stellar types are extremely rare, making up less than 1% of all stars (Ledrew, 2001). The majority of stellar continua should be free from contamination by these hot stars, and appear flat within our data.

The 34nm width of the SN3 filter tends to amplify this effect. The tiny bandpass acts to mask any macroscopic curvature present in the SED, much like how the Earth appears flat locally because our range of sight is vastly smaller than the Earth's radius of curvature. Only the hottest and brightest OB type stars would show significant deviations from a flat continuum within this wavelength range; corrections for these stars will be discussed in Section 3.3.2. Therefore, in order to locate potential LE candidates, it would be sufficient to identify regions within our data, where spectra display negatively-sloped continua.

Our continuum fitting methodology relied heavily on the optimized curve fitting

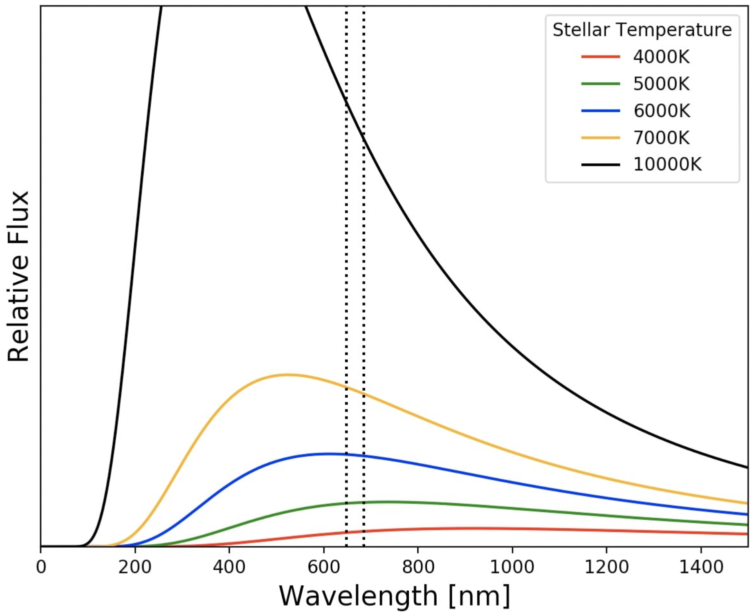

FIGURE 3.4: Blackbody energy flux curves for stars of different temperatures. The SN3 filter bandpass is shown between the two black dotted lines. Only stars with temperatures greater than 7000 K have a continuum slope which deviates significantly from zero within the filter. Stars with temperatures greater than 10 000 K have increasingly negative slopes in the SN3 filter, and are not shown for visual clarity.

framework provided by the SciPy Python package [3]. SciPy has least-squares (LSQ) fitting capabilities which can be adapted by the user for a variety of non-linear data models. For a given model, it provides a vector containing the LSQ determined values for each of the free parameters, as well as minimized error estimates. In our case, we required only a simple two-parameter fit; returning the best estimates for continuum slope and y-intercept, as well as the corresponding uncertainties.

Our datacube consists of only 49 frames. Since each frame corresponds to one single point in an extracted spectrum, 49 is the maximum possible number of data points which can be included in the fit. However, there were modifications to the data required before fitting could commence: for example, frames containing emission lines must be removed. It is clearly better to fit a larger, rather than smaller amount of data, and

[3] https://www.scipy.org

it was therefore essential to reject as few frames as possible, while ensuring that the remaining subset of frames contained solely continuum emission.

3.2.1 Frame Rejection Criteria

There were two main criteria for the rejection of a frame: the presence of emission lines, or if the frame lay outside of the 100% transmission region of the filter bandpass.

Filter Bandpass Criterion

The first criterion to be considered was the extent of the filter bandpass. Included in all SITELLE datacubes, regardless of the chosen filter, are observations of a number of frames outside of the bandpass. With SN3, approximately half of the observed frames are outside of the filter bandpass, irrespective of the spectral resolution, and contain no emission, since the instrument throughput is zero at these wavelengths. In our observations these frames account for 28 out of our 49 total frames, and must not be included in our fits.

This is an unavoidable byproduct of SITELLE's method of operation. Due to the off-axis nature of the optical elements, each pixel on the CCD corresponds to a slightly different optical path difference, resulting in the constructive interference of different wavelengths. The detected wavelength varies like $\frac{\lambda}{\cos\theta}$, where θ is the offset angle from the optical axis, and goes from 11.8^o to 19.6^o. This can result in a change in detected Hα wavelength of up to 26nm across the frame.

The wavelength variations are characterized with a laser calibration cube, where a 543nm HeNe laser source is incident on SITELLE's instrumentation and variations in the observed wavelength is measured across the CCD. The wavelength changes are corrected through altering the zero-point of the Fast Fourier Transform. In this manner, only a single wavelength will be present in each frame. An example laser calibration map is shown in Figure 3.5.

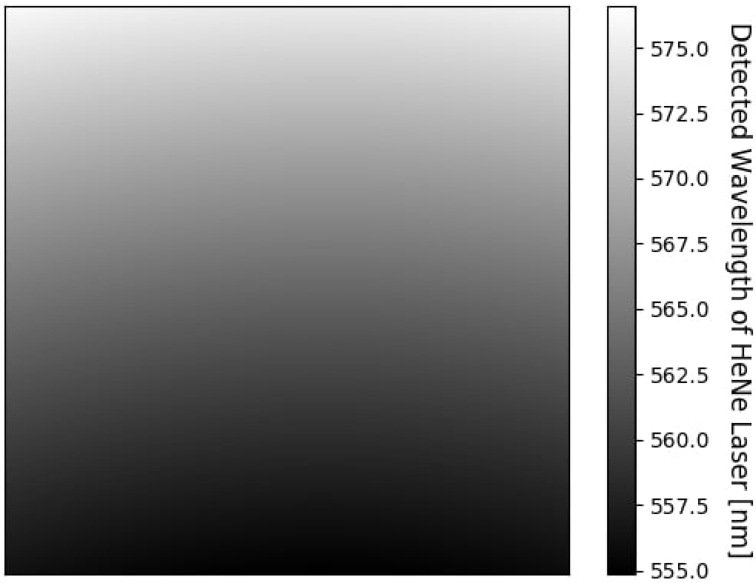

FIGURE 3.5: Laser calibration map for our datacube showing the variations across the frame in the detected wavelength of a HeNe laser (central wavelength 543 nm).

As discussed previously; even though the maximum OPD of the interferometer sets its spectral resolution, the interferogram must be properly Nyquist sampled in order to accurately reconstruct the spectrum. However, SITELLE actually samples the interferogram *below* the Nyquist rate in order to obtain the desired spectral resolution in a shorter period of time (Drissen, 2016). In our observations, the SN3 filter acts as a low-pass filter in Fourier space to prevent aliasing (the other filters also provide the same functionality if used). If an interferogram is not bandwidth limited (does not go to zero at the edges of the sampled regime) the tails of the spectrum outside the bandwidth will be folded back into the bandwidth and form aliases. The SITELLE filters ensure that the data go to zero at the edges of the bandwidth, and hence prevent aliasing.

Since the detected wavelength varies across the frame, the top of the frame (the largest offset angle) will 'see' the filter edge before the bottom. For example, the red edge of the SN3 filter is detected at 699 nm at the top of the frame, but 665 nm at the bottom. Similarly, the blue edge of the filter varies from 727 nm to 691 nm across the frame. Regardless of the spectral resolution, multiple frames need to be observed to capture the filter edges across the entire CCD. At our spectral resolution, the filter edges appear across a combined 34 frames. After wavelength calibration, 28 of these frames corresponded to wavelength regimes that are outside the filter bandpass and contain no emission - these are the frames that we rejected.

Emission Line Criterion

Moreover, the frames containing emission line complexes must be removed. NGC 6946 is a low inclination galaxy at $38^{\rm o} \pm 2^{\rm o}$ (Boomsma et al., 2008). There is some rotation perpendicular to the plane of the sky, resulting in a velocity field within the galaxy. This is visualized in Figure 3.6 showing galaxy-centric Hα line velocities, as determined by an ORCS emission line fit of the archival cube. There is a maximum velocity shift of $\sim$150 km/s across the galaxy, in good agreement with the $\sim$160 km/s reported by Boomsma et al. (2008).

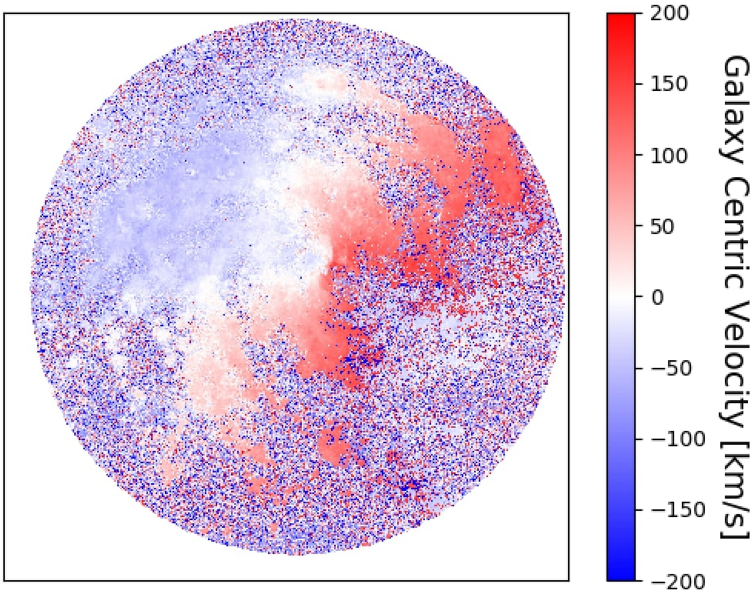

FIGURE 3.6: Map of Hα line, galaxy-centric velocity across NGC 6946. The galaxy's rotation is visible, with a maximum range in velocity of $\sim$150 km/s.

With the standard conversion formulae:

$$\sqrt{\frac{c+v}{c-v}} - 1 = z = \frac{\Delta\lambda}{\lambda_0} \tag{3.1}$$

we can convert this velocity to a shift in the spectral line wavelength. In Equation 3.1, v is the line-of-sight velocity, c is the speed of light, z is the redshift, and λ_0 is the rest frame wavelength of the spectral line.

In the archival cube, this evaluates to a maximum wavelength shift of 0.32 nm at the wavelength of Hα. With a frame step size of 0.3 nm, this would result in the Hα line being displaced by more than an entire frame on one side of the galaxy compared to the other. However, due to our low resolution and an average frame step size of 2.2 nm, the line complexes will never shift out of the same frame in which they would be located if at rest. This makes the job of subtracting emission line frames much easier. Eight frames containing the 'Hα, [NII]654.8, 658.4' complex, as well as the '[SII]671.7, 673.1' complex were identified and removed.

This leaves a total of only 13 frames out of 49, which contain solely continuum emission - these are the frames which can be included in the continuum fitting procedure. With only 13 data points there is a severe risk of over-fitting - in inferring the presence of a LE where in reality there is only noise. To quantify this risk, we employed two statistical tests to ensure that negative slopes present in the continuum were indeed statistically significant.

3.2.2 The Statistical Tests

Two different, but related statistical criteria were applied to ensure the significance of a negatively (or positively) sloped continuum over the null-hypothesis (flat continuum): the Akaike Information Criterion and the Bayesian Information Criterion, hereafter AIC and BIC respectively. The AIC, proposed by Akaike (1973), is a statistical estimator to gauge a model's goodness of fit to a specified dataset. It weighs both the goodness of fit, and the risk of over-fitting. The AIC is generally calculated via

$$AIC = 2k - 2\ln\hat{L} \tag{3.2}$$

where k is the number of parameters, and $\hat{L}$ is the maximum likelihood function of the model. However, for small sample sizes it has been found the AIC tends to select models that over-fit the data (McQuarrie & Tsai, 1998, Claeskens & Hjort, 2008). To circumvent this, Cavanaugh (1997) proposed a corrected AIC formulation, which was adapted by Gordon (2015) for parameters specifically determined through linear regression:

$$AIC = n\log(\hat{\sigma_n}) + 2k + 2\frac{k^2+k+1}{n-k-1} \tag{3.3}$$

The above is suitable for small sample sizes, provided the model is linear in its parameters. Here, n is the number of data points, k is the number of parameters, and $\hat{\sigma_n}$ is the variance in each parameter.

The BIC is closely related to the AIC, but imposes higher penalties on the number of parameters that a model contains (Schwarz et al., 1978). With the assumptions that the model errors are independent and roughly distributed in a Gaussian manner, the BIC can be calculated via:

$$BIC = n\log(\hat{\sigma_n}) + k\log(n) \tag{3.4}$$

where the variables represent the same quantities as above.

The formulae in Equations 3.3, and 3.4 are remarkably similar. The BIC imposes a higher $k\log(n)$ penalty for each parameter as opposed to the $2k$ penalty in the AIC. Nevertheless, studies have found that the small-sample corrected AIC is more accurate than the BIC (Anderson & Burnham, 2004, Burnham et al., 2011). When BIC and AIC values are known for a number of competing models, the model which minimizes its information criteria is selected as the most likely to accurately represent the data. In the case of the AIC, the probability, P, that a given model accurately fits the data can be calculated by:

$$P = e^{-\Delta AIC/2} \tag{3.5}$$

where $\Delta AIC = AIC_m - AIC_0$; the difference between the AIC value of the given individual model (AIC_m), and the minimum AIC of the best fitting model (AIC_0). A ΔBIC value can be calculated in an identical manner. The statistical implications of the ΔBIC value are summarized in Table 3.2.

Table 3.2: Statistical implications of ΔBIC values on the number of parameters in a model (Kass & Raftery, 1995).

ΔBIC	Evidence Against More Parameters
0 - 2	None
2 - 6	Positive
6 - 10	Strong
>10	Very Strong

In order to test the statistical significance of any continuum slope, a sloped (two-parameter) and flat (one-parameter) model was fit to the extracted spectra. The BIC and AIC values for each model were compared in the following manner:

$$\Delta AIC = AIC_{2p} - AIC_{1p} \tag{3.6}$$

$$\Delta BIC = BIC_{2p} - BIC_{1p} \tag{3.7}$$

A negative value for each criterion, indicates that the two-parameter fit is most likely. In particular, values of $\Delta\text{BIC} < -2$ and $\Delta\text{AIC} < 0$ were our requirements for a statistically significant sloped continuum. If the statistical tests did not meet the above criteria, the continuum was deemed to be consistent with flat.

3.2.3 Putting Everything Together

The fitting methodology is summarized in Figure 3.7. A high S/N HII region spectrum, with prominent emission line complexes was selected as a toy model to test our procedure.

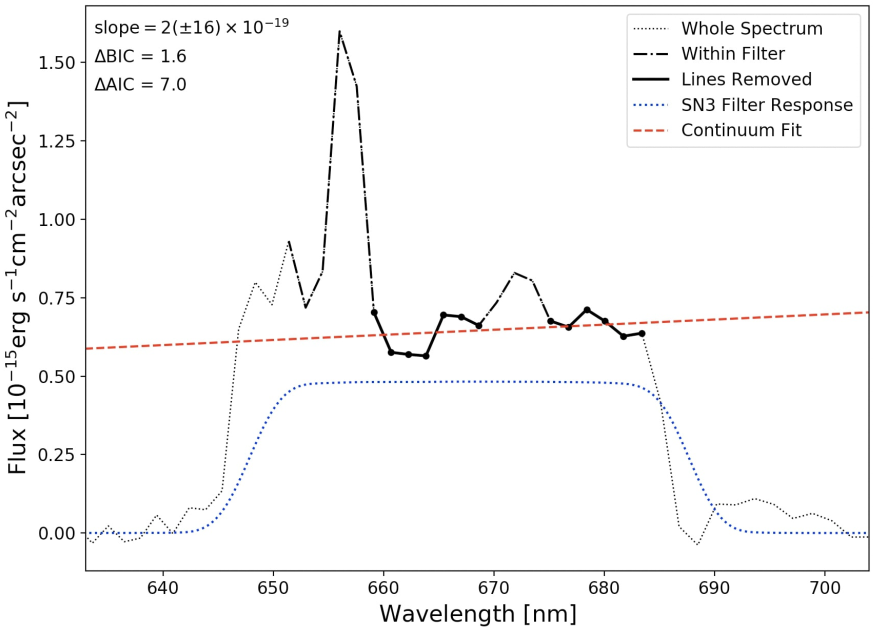

FIGURE 3.7: An example of testing our fitting methodology with a toy spectrum. The dotted black line displays the sky subtracted spectrum. The dashed black line shows the portion of the spectrum lying within the SN3 bandpass. The blue dotted curve shows the SN3 filter bandpass, with arbitrary overall scaling, for comparison. Once the spectral line complexes are removed, the remaining spectrum is shown in the solid black line, with the 13 individual frames as black dots. The best fitting two-parameter model of the continuum is shown with the red dashed line. The fit slope, as well as ΔAIC and ΔBIC values are included in the top left corner.

Even in this well behaved, and comparatively high S/N spectrum, the continuum is quite noisy. This emphasizes the need for the aforementioned statistical criteria. The best fit two-parameter model displays a slope of $(2 \pm 16) \times 10^{-19}$erg/s/cm^2/arcsec^2/nm. The large error reflects the scatter present in the continuum. This particular region did not pass even the first test in validating negatively-sloped continua - its large error bars rule it out. However, supposing it did make this first cut, it has positive values of both ΔAIC and ΔBIC, which confirm that the one-parameter model is most likely. In fact, by applying Equation 3.5, the two-parameter model is only 3% as likely to accurately fit the data compared to a one-parameter model. Ergo: this continuum is consistent with flat.

There is also one additional test that can be performed, made possible by our access to the archival datacube. We proposed observations at 279 seconds per interferometer step. The data we received only reached a third of this depth, effectively 93 s/step. This however, is still three times deeper than the archival cube. We would expect that the archival cube, with its shallower exposure will be sensitive almost solely to the stellar continuum, whereas the depth of our observations will give us information about the stellar continuum, combined with potential LEs fainter than the magnitude limit of the archival cube. If we see a negatively sloped continuum in our data, but a flat continuum in the same region in the archival data, this is a good indication that this slope is *not* due to stellar continuum, and further evidence for the presence of a faint scattered LE.

3.3 Understanding Systematic Biases in the Data

The following section will illustrate various corrections that were required, or considered before the results can be discussed.

3.3.1 Sky Subtractions

All spectra were sky subtracted before any continuum fitting was attempted. Naively, in preliminary analyses of spectra, a region of dark pixels in the corner of the frame was chosen as the sky region, and used to uniformly correct spectra across the entire frame. These initial sky-subtracted spectra showed pointed irregularities, as displayed in Figure 3.8.

There are enormous spikes in emission visible at both edges of the filter bandpass, and these spikes increase in intensity as the region from which the spectrum was extracted moves closer to the centre of the frame. Upon deeper inspection of the datacube, we

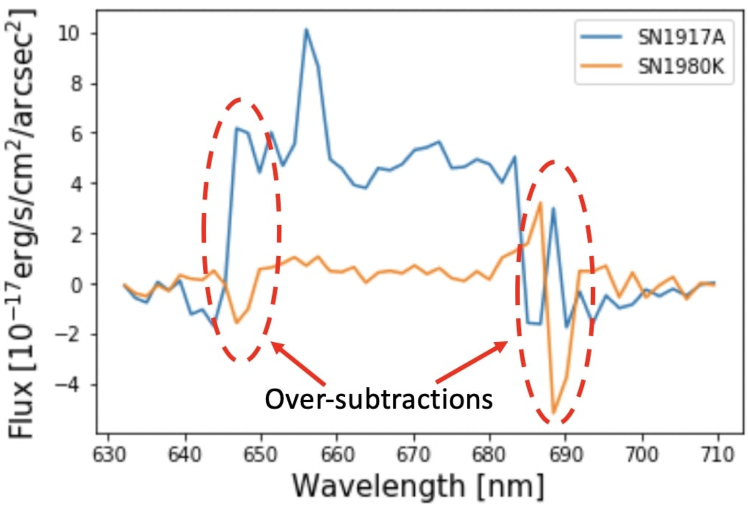

FIGURE 3.8: Examples of sky over-subtractions in spectra with low and high continuum flux levels.

discovered an anomalous brightness pattern in the frames at the edges of the filter bandpass. As shown in Figure 3.9, a frame at the very red edge of the SN3 filter, the outskirts of the frame are brightest whereas the centre is comparatively dark. A region at the edge of the frame was chosen for the sky subtraction specifically because it should be the darkest; significantly offset from the galaxy which we expect to be the source of the vast majority of the emission - however this is not what we are seeing in these frames.

We determined two root causes for these so called 'filter edge effects': the presence of bright sky lines, and the differential response curve of the filter itself.

There are a number of bright sky lines within the SN3 filter, as can be seen in Figure 3.10 from the archival NGC 6946 datacube. From the Osterbrock et al. (1996) catalogue of night sky lines above Mauna Kea, there is a very intense OH line at 686.3 nm, as well as another group of less intense, but densely packed lines from 644 to 648 nm. These individual lines are resolvable in high resolution data, however with our low spectral resolution, these densely packed lines are all present in a single frame, and are effectively combined into one intense emission line. This explains why these edge-of-filter frames

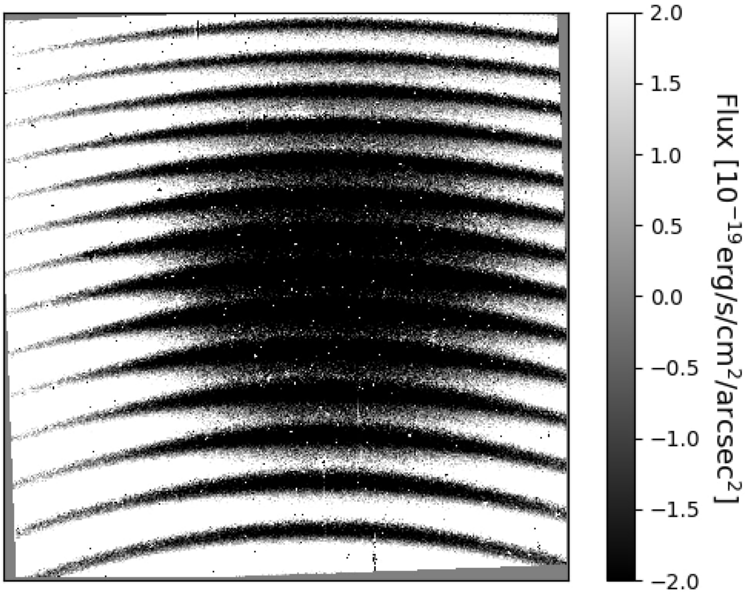

FIGURE 3.9: The 14$^{\text{th}}$ frame in the datacube, at the red edge of the filter bandpass. The outskirts of the frame are much brighter than the frame centre, where the flux level dips to unreasonable negative values. Dark arc patterns (possible artifacts from the phase calibration) are also visible, and will be discussed further in Chapter 3.3.3.

are so bright, but does not address why we only see the emission at the edges, as opposed to uniformly across the frame.

The reason for this last variation in brightness is the differential response curve of the SN3 filter, displayed in Figure 3.11. For a perfectly collimated incident beam, each ray impacts the filter at the same incidence angle, namely normal incidence. However, if there are inaccuracies in the collimation, there will be rays hitting the filter at various incidence angles, and these non-normally incident rays will tend to impact the *edges* of the filter, compared to collimated light which will impact uniformly across the frame (e.g. Figure 3.12).

The response curves show that for angles of incidence greater than normal, the filter 'sees' longer wavelengths of light. Similarly for incidence angles less than normal, the filter 'sees' shorter wavelengths of light. The combined effect of bright emission lines near the edges of the filter bandpass, as well as the filter 'seeing' high and low incidence

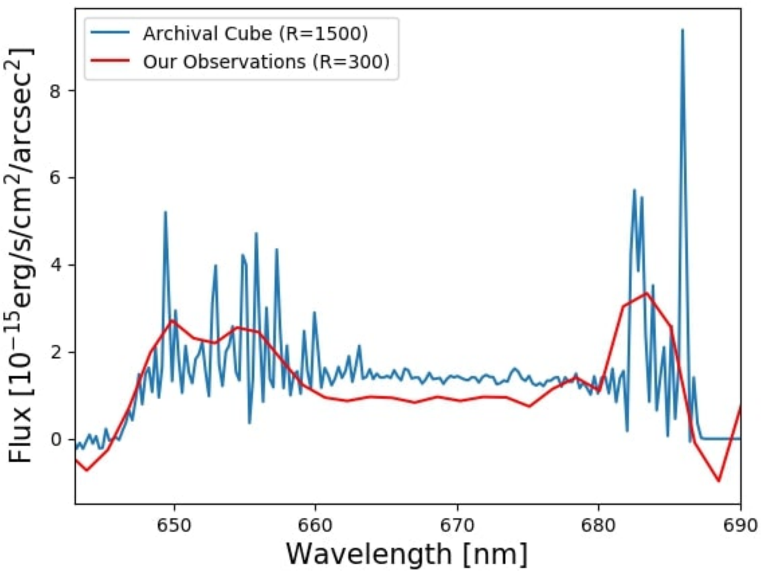

FIGURE 3.10: Comparison of sky lines present in the SN3 filter in our observations, and the high resolution archival cube. There are bright OH-band lines at both edges of the filter.

angles before normal rays as it scans through its waveband, perfectly describes what is seen in Figure 3.9. This would subsequently be reflected in sky over-subtraction at the edges of the filter, increasing in intensity moving towards the frame centre - which is exactly what we see.

In order to correct this effect in our spectra, a variable sky region method was tested. We fit ten isophotes to the edge-of-filter flux, corresponding to roughly 10% decreases from maximum brightness. The edge-of-filter flux was determined simply by using only the frame of the datacube encompassing the red edge of the filter (e.g. Figure 3.9). Within each isophote, an overall darkest region was selected from the deep frame as the 'sky', and then used to correct all other pixels within that isophote. The initial spectra using this method were promising. Figure 3.13 shows the same regions as in Figure 3.8, before and after correction with the variable sky method. The edge effects are removed, with minimal effect on the rest of the spectrum.

Unfortunately, once this method was applied to the entire cube it became clear that

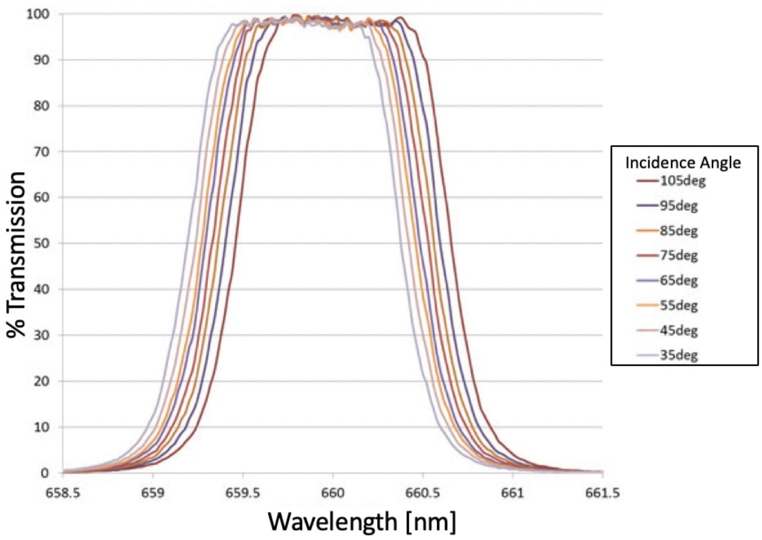

Figure 3.11: Variation in the transmission response for the SN3 filter for incident light with angles within 25° of normal. The filter reaches 100% transmission for lower and higher wavelengths before the central wavelength - essentially it 'sees' these wavelengths first.

we had underestimated the errors we were introducing. Figure 3.14 shows the slope of the continuum, as determined by our continuum fitting methodology, across the whole galaxy. Immediately obvious is the ringed structure in the background, directly mirroring the ten edge-of-filter isophotes - the sky subtraction left unanticipated, high level artifacts in our data.

To understand these artifacts further we compared the effect on the slope of the continuum fit, as well as the two information criteria, of using the variable sky subtraction method as opposed to just using one of the five darkest regions of the frame - each region consisting of 30 pixels. Figure 3.15 displays the results of this analysis on the slope, and ΔBIC parameter. It is obvious that the variable method imposed the most negative slopes on the data, compared to all other sky options. As progressively darker sky regions are used, the resulting continuum slope becomes increasingly positive.

Trends in the ΔBIC value are more difficult to disentangle, however the S/N of the

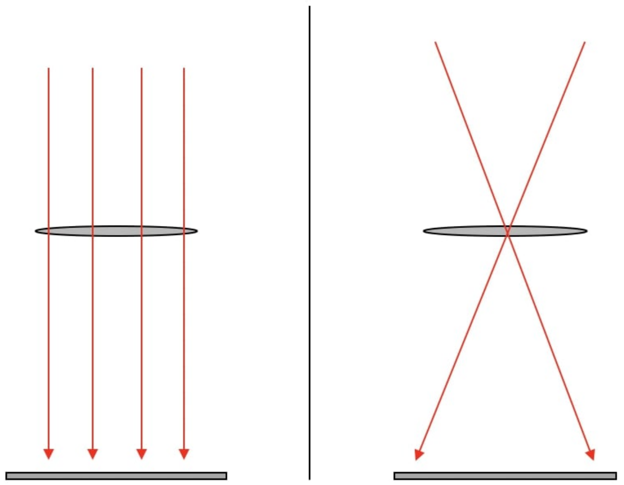

FIGURE 3.12: Schematic comparison of the differences between perfect and imperfect collimation. Perfectly collimated light will be normally incident, and evenly distributed across the frame (left). If there are some imperfections in the collimation, this light will preferentially hit the edges of the frame (right).

spectrum selected likely plays a significant role. The curves with the highest amount of fluctuation tend to have a lower S/N level than curves with less variation across all sky subtractions. Lower S/N regions would be more susceptible to the choice of sky, and the resulting continuum fit will be more volatile. In contrast, effects of a sky subtraction on the high S/N regions would be nearly negligible, leading to the relative consistency of their fit information criteria.

It was clear that using a variable region for sky subtraction needed to be abandoned. Through the removal of frames outside the filter bandpass though, our continuum fitting methodology ignores the portions of the spectrum affected by the over-subtraction. After weighing the errors introduced by the variable sky method, against what was reduced to purely aesthetic benefits, it was clear that returning to a sky subtraction using the darkest pixels would minimize any artifacts introduced into our data. All subsequent results and maps were produced using a single sky region.

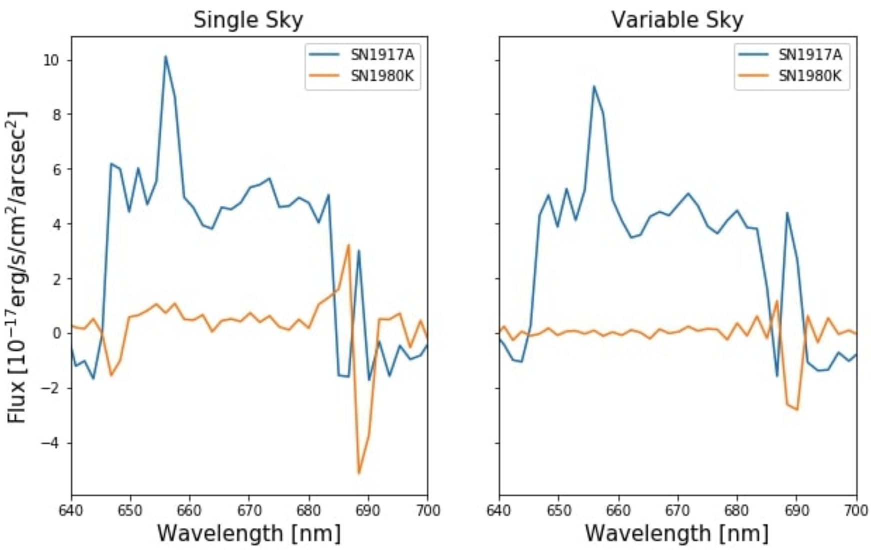

Figure 3.13: Comparison of spectra before and after correction of the edge effects with a variable sky selection method. The left side shows the same regions as Figure 3.8. The right side of the figure shows these same regions, but now corrected with a sky specifically chosen to mitigate edge effects. With the new skies, the over-subtractions at the filter edges are minimized, with negligible changes to the rest of the spectrum.

3.3.2 Masking of Bright Stars

NGC 6946 is classified as a starburst galaxy, and its myriad HII regions, as well as other star forming regions are clearly visible and well studied (Schinnerer et al., 2006). This is problematic for our study because unlike the continuum emission of older stellar populations, which appear flat in the SN3 filter, young and hot, OB type stars living in these HII regions and OB associations will manifest themselves as strong negative slopes in the SN3 filter continuum. This introduces an unwanted degeneracy over the root cause of statistically significant negative slopes in our continuum measurements: is it a LE candidate, or simply a hot star? This unfortunately is unavoidable - by nature of containing the hottest and most massive stars, OB associations are also some of the best places to find core-collapse SNe.

Luckily, there are straightforward methods that can be applied here. Figure 3.16 shows the continuum slope across the frame, identical to Figure 3.14 except using a

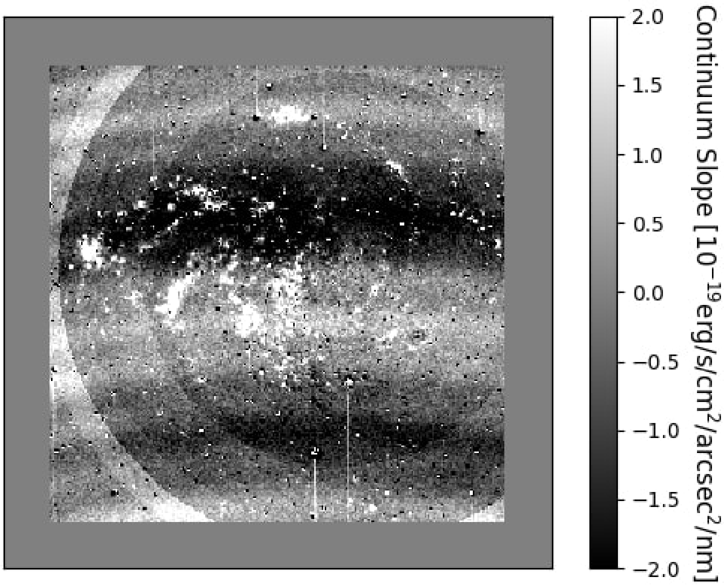

FIGURE 3.14: Map of continuum slopes across the frame after the application of the variable sky subtraction method to mitigate edge effects. There are rings visible in the background, which correspond to the edges of isophotes used to determine the different sky regions. This is clear evidence that we underestimated the errors being introduced through this method.

single sky region (note the lack of rings in the background). Due to the depth of our observations, the very brightest of stars are saturated, and display prominent diffraction lines that contaminate the data. These are easily identifiable and a pixel mask was manually constructed to not only mask the point spread function (PSF) of the saturated stars themselves, but also the diffraction peaks.

Also visible in Figure 3.16 are a multitude of bright stars that did not saturate the CCD - notably they show up as dots with extreme negative slopes, exactly as predicted. In addition to these stars, the continuum slope data seems to also be tracing the interstellar medium (ISM) of the galaxy. The spiral arms are roughly outlined, betrayed mostly by the presence of the many HII regions. These regions also need to be masked - it is nearly impossible that we will find a LE buried in the bright emission of these regions. This unfortunately means that our methodology contains a bias against LE

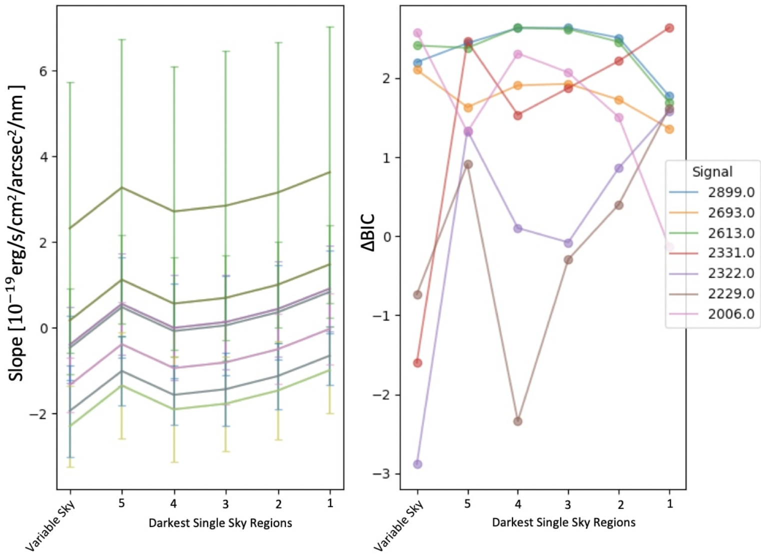

FIGURE 3.15: Effects of using different regions for sky subtraction on the continuum slope and ΔBIC parameter. Seven random regions were corrected with six different sky regions, and put through the continuum, fitting procedure. The variable sky method has biased slopes more negatively than using any of the five darkest regions in the frame for a single, constant sky subtraction. Using the darkest region in the frame yields the most positive slope in the continuum. The effect on ΔBIC is likely tied to the S/N level in the region being fit. Regions with the lowest signal show large variations in the ΔBIC parameter, whereas higher signal regions show less variation. This can be explained by a region with a low S/N being more sensitive to the choice of sky, whereas a sky subtraction is merely a small perturbation on a high S/N region.

detection in areas of high emission.

To simultaneously remove the saturated and bright stars, as well as the HII regions from our analysis, an overall pixel mask was created combining the saturated star mask and a second mask including all pixels with flux >5000 erg/s/cm^2/arcsec^2 in the deep image. This corresponds to roughly the brightest 1.5% of pixels, and includes all background and foreground stars, as well as HII regions and OB associations. It also has the added benefit of masking the galactic centre.

Prior to this blanket cut of pixels, PSF subtraction of the brightest stars was attempted with the publicly available SExtractor software package[4]. SExtractor models

[4]https://www.astromatic.net/software/sextractor

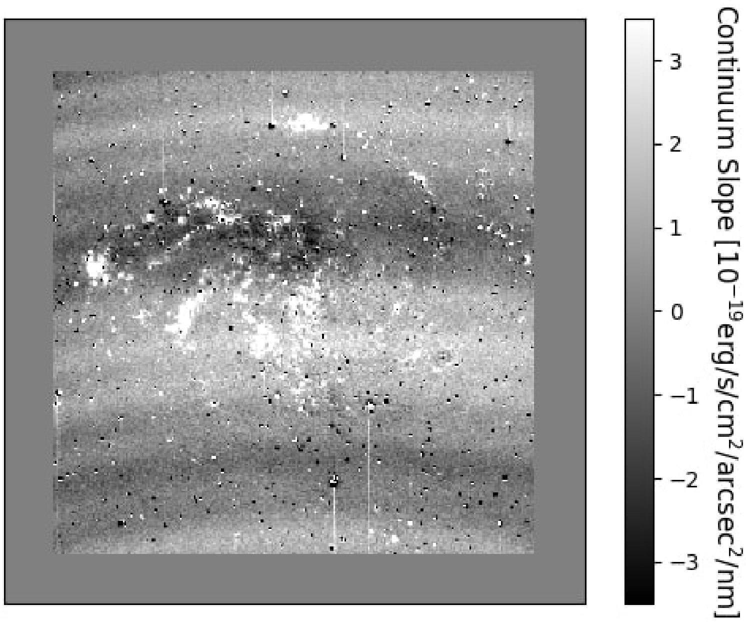

FIGURE 3.16: Map of continuum slopes across the frame after the application of a constant sky subtraction with the darkest region of pixels in the frame. The rings that were previously visible are now gone, however there are other artifacts (e.g. saturated stars, phase calibration arcs) that need to be removed.

and subtracts the PSFs of stars in an image, down to a user specified limit. However, it struggled with our dataset for two reasons: our image depth, and SITELLE's PSF distortion. First, as already discussed, the depth of our observations led to widespread saturation. SExtractor was unable to accurately detect stars buried within the bright swath of emission around HII regions, or in the neighbourhood of saturated stars. Furthermore, SITELLE is known to have increasingly distorted stellar PSFs in the frame corners. This distortion is thought to be due to misalignment and manufacturing defects in the mounting and camera, and is relatively well characterized. However, no standard corrections had yet been implemented at the time of our observations. As expected, SExtractor also struggled in modelling the highly distorted, coma-like, PSFs far from the frame centre. Given these difficulties and the lack of obvious solutions, we abandoned the use of SExtractor, and moved to simply exclude pixels above a flux limit.

When running the continuum fitting procedure, pixels were binned on a 7×7 scale in order to increase the S/N. An integrated spectrum was extracted over the 49 pixels in each bin, and the results of the fit were assigned to the entire binned region. This scale also corresponds to approximately the size of SITELLE's nominal PSF, meaning structure on any smaller scales is likely dominated by noise. Therefore, no information is lost through this binning. During the binning, pixels which were to be masked were rejected, and not included in the integrated spectrum of that region. If more than 50% of the region's pixels were masked, the region as a whole was rejected. Out of 64009 binned pixels, 4997, or 7.9%, were masked.

This masking is the final modification made to the datacube before applying the continuum fitting procedure, the results of which will be discussed in Chapter 4.

3.3.3 Phase Calibration Artifacts

One final correction was attempted on the continuum data *after* running the fitting procedure. In Figure 3.16 the ringed pattern previously present has been corrected, however horizontally arced stripes are now quite prominent in the background.

The arc pattern in our slope data, exactly matches the angle traced out in the laser calibration map (Figure 3.5), clearly indicating that what we are seeing in our data is an instrumental effect - perhaps left over from the laser calibration, or phase correction. The phase correction uses astrometric measurements of background stars to line up the images produced by the two complementary detectors in SITELLE. It is known that ORBS has had difficulties in applying phase corrections to datasets with very low spectral resolution (Prunet, 2019). However, Liu (2019) has also noticed these artifacts in their observations of Abell 2390, despite having a higher spectral resolution.

We attempted a solution using the laser calibration frame, the result of which is shown for the continuum slope map in Figure 3.17. Following the interferometer angle, we identified 'sky-pixels' within half-degree wavelength increments of the laser calibration map, as all pixels in the deep frame with flux <1500 erg/s/cm^2/arcsec^2. The median slope of the sky pixels in each wavelength range was subtracted from all pixels within that range. The median error of the sky pixels was also added to the error in the continuum fit for each pixel.

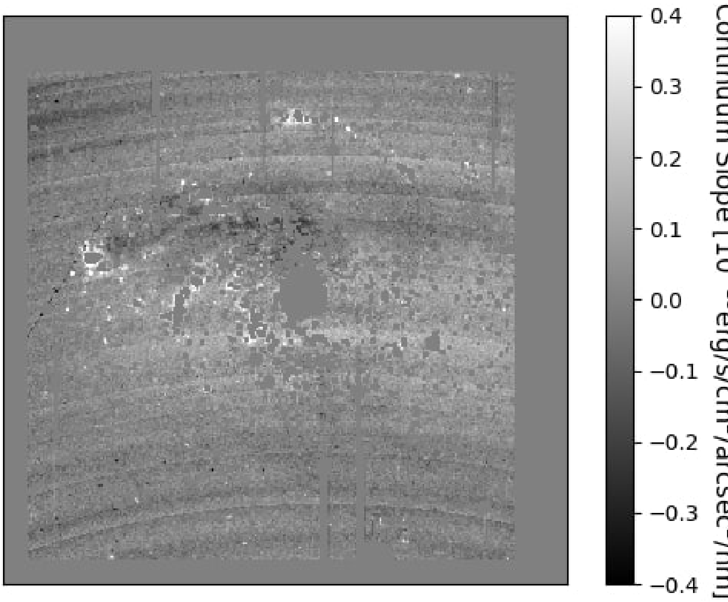

FIGURE 3.17: Map of continuum slopes across the frame after the attempted phase calibration correction using the laser map. The background is more homogeneous, but the arcs are still present - now on smaller pixel scales.

There are two difficulties with this attempted correction, beyond the fact that it doesn't bring us any closer to understanding why these artifacts are present in the first place. The background arcs still remain, but now their size reflects the half-degree scale on which the corrections were applied. We have mostly removed the instrumental artifacts, but introduced new artifacts in their place. The larger issue is that there is no clear manner in which to correct either the ΔBIC or ΔAIC parameters. One cannot just subtract off the median statistical parameter of the sky pixels. With these considerations, we elected to accept these instrumental errors moving forward, and work to understand and quantify their effects on our final results. Moving forward, all maps and results that will be discussed in the next chapter do not include this laser map correction.

Chapter 4

Results

4.1 Searching for Light Echoes from the Ten Supernovae

It is possible, and indeed likely, that there are more unrecorded SNe in NGC 6946 which predate SN 1917A. However, we have no way of knowing how long ago, and where these historical SNe would have erupted. In which case, it is reasonable to start our search for LEs in NGC 6946 with the regions immediately surrounding each of the ten recorded SNe.

4.1.1 Analysis of Individual Supernova Regions

There are no detailed dust maps of NGC 6946 to guide our search for LEs, and as such we had to search the entire area over which it would be possible to find a LE from each SN. From the known geometry of scattered LEs, there is a maximum projected area around the SN epicentre within which it is theoretically possible for a LE to be found - this of course wholly depends on the existence and favourable positioning of scattering material within this area.

The radius of the circular area is determined through use of Equation 1.3 - the LE equation. In addition to the age of the SNe, and the 7.72 Mpc distance to NGC 6946, an assumption needed to be made about the dust height above the galactic plane, z, in order to calculate the projected radius, ρ. The thin disk contains most of the galactic dust, so we assumed a thin disk scale height of 0.25 kpc for NGC 6946 - comparable to that of the MW (Carroll & Ostlie, 2017). This scale height represents the maximum height above the galactic plane within which we could reasonably expect scattering dust to exist.

With these assumptions, we determined the projected LE search area for each of the ten SNe. An integrated spectrum was extracted from each region for further examination for evidence of any LE candidates. Spectra of each region are displayed in Figure 4.1, along with comparison spectra of the same regions in the archival cube.

We fit the continuum in each of the extracted spectra to determine whether any of these regions displayed the characteristic negative slope that we anticipate will indicate the presence of LEs. The region parameters, and results of the continuum fitting are summarized in Table 4.1.

TABLE 4.1: Summary of the parameters, and continuum fitting results from the initial search regions around the ten recorded SNe

Designation	Radius (arcseconds)	Radius (pixels)	Slope (erg/s/cm^2/arcsec^2/nm)	ΔBIC	ΔAIC
1917A	3.43	12	3.4(6.5)e-19	2.3	7.7
1939C	3.01	10	2.22(5.73)e-18	2.5	7.8
1948B	2.82	10	-4.8(4.9)e-19	1.5	6.8
1968D	2.37	8	3.1(4.8)e-19	2.2	7.5
1969P	2.35	8	-2.85(2.39)e-19	1.1	6.4
1980K	2.06	7	3.09(3.28)e-19	1.6	7.0
2002hh	1.33	5	-6.18(5.03)e-19	1.0	6.3
2004et	1.24	5	1(10)e-20	2.6	8.0
2008S	1.05	5	-10(7)e-20	0.6	6.0
2017eaw	0.33	4	-1.12(0.52)e-18	-1.9	3.4

Pixel radii are convolved with the nominal 3.5 pixel PSF radius, and rounded to the nearest whole number.

There is nothing immediately obvious in any of the spectra that suggest the presence of a LE. Two of the regions, SNe 2017eaw and 2002hh, display very significant emission lines. This can be explained by the proximity of each of these SNe to HII regions which completely dominate the local emission. Furthermore, we do not expect bright emission

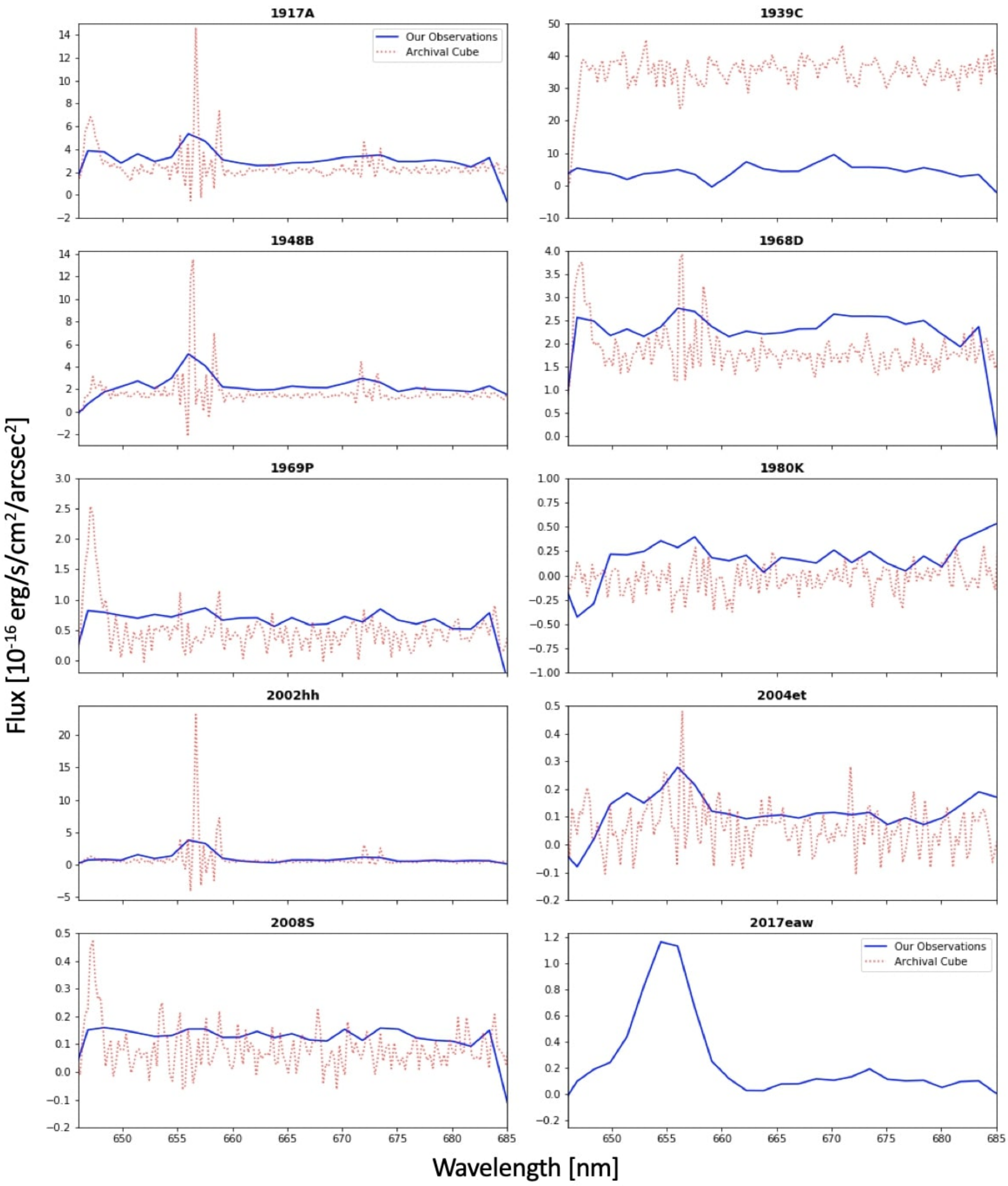

Figure 4.1: Spectra of the region surrounding each of the ten recorded SNe. Spectra of the same region in the archival cube is shown for comparison. The archival spectrum of SN 2017eaw is omitted as the SN was still in its outburst phase during those observations.

lines to be characteristic of LEs, which we would expect to see in highly broadened, continuum-like emission. There is also a saturated star blocking the location of SN

1939C, which contaminates its spectrum.

The continuum fitting results also confirm the lack of clear evidence for SN LEs in any of these regions. None of the ten regions meet the criteria of having a continuum slope that can only be negative within error, as well as values for the statistical criteria of ΔBIC < -2 and ΔAIC < 0. All of the continua are consistent with being flat.

4.1.2 Comparison with the Galactic Mean Spectrum

It is likely that LE effects would be subtle, and not be immediately obvious in a spectrum of one single region. In order to tease out any possible evidence for LEs in these aforementioned regions, we sought to make a comparison with the mean spectrum of the galaxy.

To gain S/N, the spectra of nine of the ten SN regions were co-added to create the so-called 'Integrated Potential LE Spectrum'. SN 1939 was omitted due to the saturated star contamination. In order to create the mean galactic spectrum, spectra from nine regions of identical size to the SN regions were randomly extracted and co-added. This was repeated 50 times, and the mean of all 50 spectra was taken to be the 'Mean Galaxy Spectrum'. The comparison of the two spectra is shown in Figure 4.2.

Unfortunately, there was once again no clear difference between the potential LE spectrum and the mean galaxy spectrum indicative of the presence of LEs. The generally stronger emission in the Integrated LE Spectrum can be explained by the proximity of many of the SNe to very bright HII regions.

The continuum fitting results also do not reveal any differences between the two spectra. The mean galactic continuum has a slope of $1.69(\pm 2.10)\times 10^{-18}$erg/s/cm^2/arcsec^2/nm with statistical criteria ΔBIC $= 1.9$, and ΔAIC $= 7.3$. The potential LE spectrum has a continuum slope of $-2.21(\pm 2.34) \times 10^{-18}$erg/s/cm^2/arcsec^2/nm, with ΔBIC $= 1.6$ and ΔAIC $= 7.0$. Both continua are consistent with flat based on the criteria that we have used.

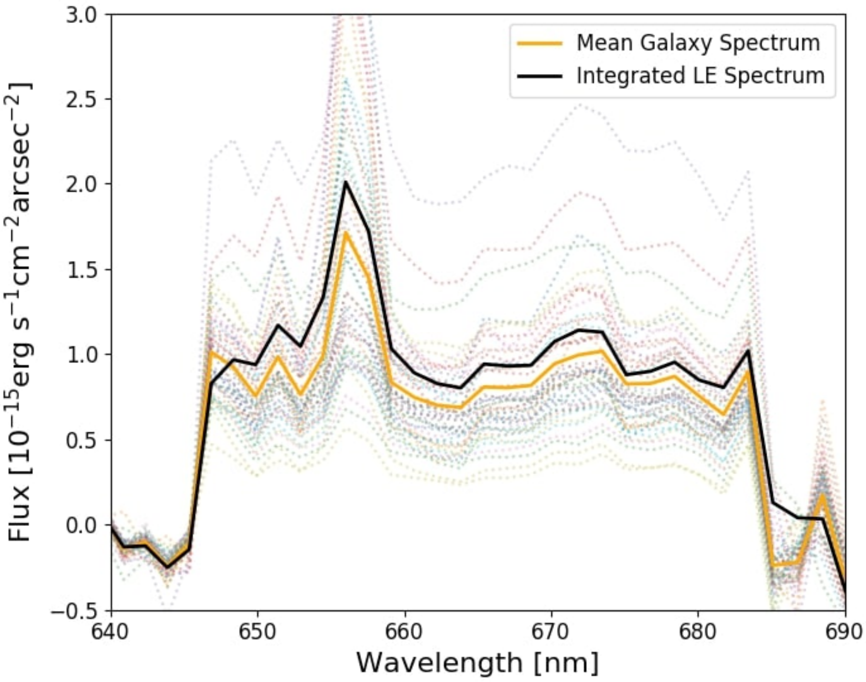

FIGURE 4.2: Comparison of the Integrated Potential LE Spectrum with the Mean Galactic Spectrum. Faded lines in the background represent the spectra of each of the 50 regions making up the mean. There is no clear difference in the continuum between the two spectra. Generally stronger emission in the Integrated LE Spectrum can be ascribed to the proximity of many of the SNe to very bright HII regions.

It was always unlikely that many of the more recent SNe would produce resolvable LEs, as simply not enough time has elapsed since eruption. Saturation also contaminated SN 1939C, which being the second oldest SN, could have resolvable LEs. No evidence for the previously discovered LEs from SNe 2002hh and 2004et were found either - both likely confounded by insufficient spatial resolution and observation depth. The SN 2002hh LE especially was victim to our bias against detecting LEs in regions of high-emission. In our observations, the area within which the 2002hh echo was found is dominated by emission from the neighbouring HII region - making recovering the LE nearly impossible. The original study of Welch et al. (2007) was able to overcome this difficulty by having both the emission and absorption component of the P-Cygni profile in the Hα line present in their spectra. Lacking the absorption component, any P-Cygni profiles would look identical to hot stellar continuum in our data, making LE detection nearly impossible in these regions.

We could now move on to search the remainder of the galaxy for evidence of LEs from SNe greater than a century old, which would be resolvable at our spatial resolution.

4.2 Searching for Light Echoes from Historical Supernovae

As already stated, it is entirely possible that within NGC 6946 there are a suite of detectable LEs from SNe predating the discovery of SN 1917A. Searching for negatively-sloped continua throughout the rest of the galaxy then serves a dual purpose: it could yield LE candidates from such historical SNe, and even if none are found it will serve as a calibration for the false-positive detection rate for our continuum fitting search strategy.

As described in Chapter 3, the filter edges and emission lines were removed from the spectra. Bright stars and emission regions were also masked before the continuum was fit with both a one, and two-parameter model. The BIC and AIC were employed to determine the statistical significance of the continuum fits.

The laser-map correction was rejected for a number of reasons which will be further discussed later in this chapter. However, the main consideration was that it was considered better to have one single instrumental artifact, instead of two: those introduced by the correction (e.g. Figure 3.17) as well as the residual instrumental errors. The final maps of continuum slope, error in continuum slope, ΔBIC, and ΔAIC are shown in Figure 4.3.

All four maps are fairly uniform - the major features being the instrumental artifacts. This uniformity is to be expected; the vast majority of pixels should hold only stellar emission, yielding flat continua with relatively small errors. This is precisely what is seen. The masked regions have been filled with an interpolation of the surrounding pixels, which adds to the smooth nature of the images.

Some features of the galaxy remain visible in the slope map - namely some of the star-forming ISM is traced. It is unclear why some of these features appear so strongly in this map, however it is notable that the same regions have the largest values in the

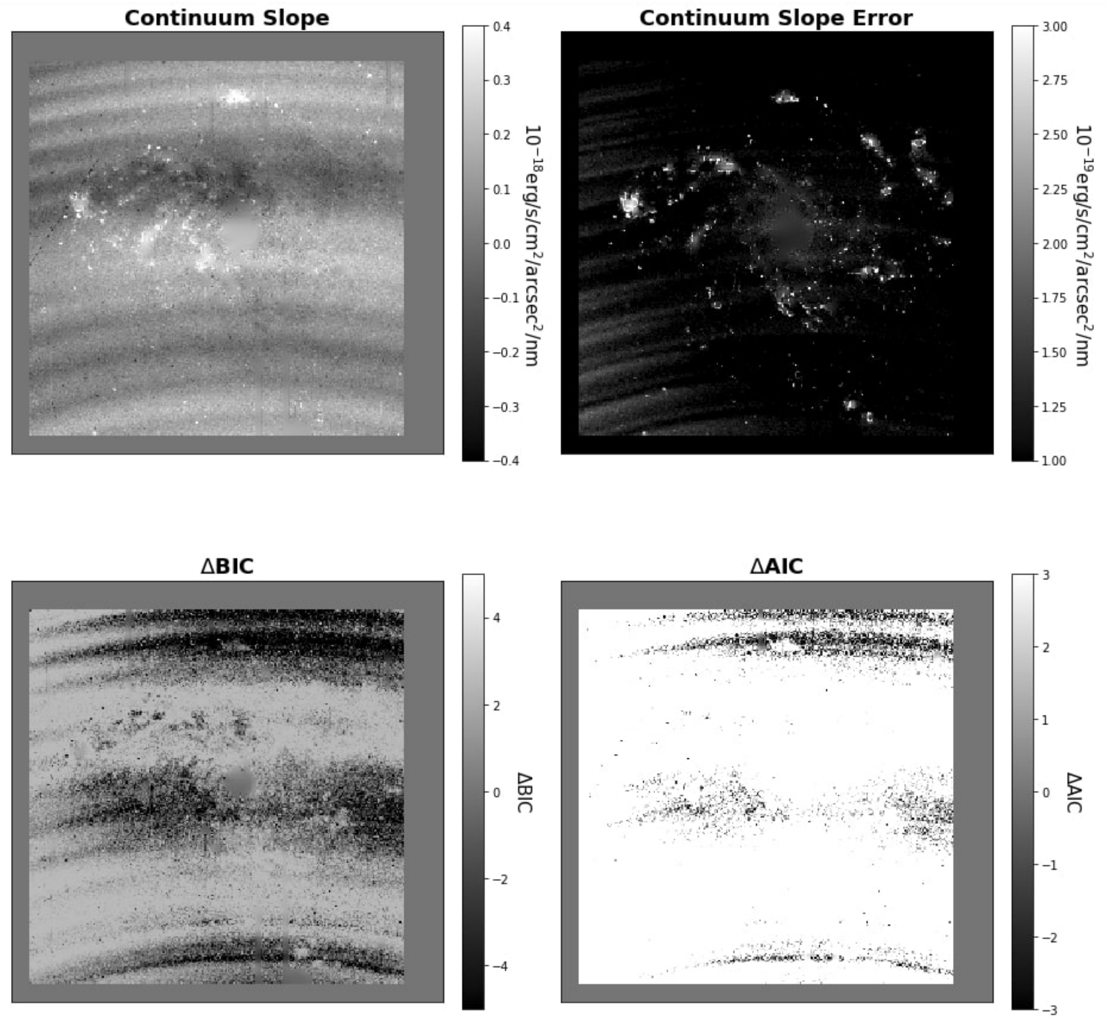

FIGURE 4.3: Maps of the continuum slope, error in continuum slope, ΔBIC, and ΔAIC parameters for each 7×7 binned pixel in the frame. The masked areas have been filled with an interpolation of the surrounding pixels.

error map. So even though some regions of the ISM appear to have largely sloped continua, these same regions also have the largest slope uncertainties, keeping the continuum slope consistent with flat.

The two areas of the galaxy which appear to have the most positive and most negative slopes (in line with, and just above the galactic centre respectively) also coincide with the most positively and negatively sloped artifacts in the frame. This is likely a large contributing factor to why we see the ISM present in these maps.

The instrumental artifacts do seem to introduce the same bias in each of the four maps. Regions of the ΔBIC and ΔAIC frames with the most significant sloped continua overlap, although the ΔAIC map is much more restrictive. The three main regions where significant sloped continua are found match the distribution of the instrumental artifacts, but for the purposes of this study it is noteworthy that these regions overlap with positively-sloped biases in the slope map. Therefore, although roughly half of the frame has been biased to negative, and half to positive slopes, only the positive sloped biases seem to be statistically significant.

Figure 4.4 shows the same four frames, but for the archival datacube. All four frames are almost completely uniform and consistent with flat continuum across the board. The ΔBIC and ΔAIC frames barely show any regions with statistically significant sloped continuum. This reinforces our expectation that the shallower observations in this data would be almost solely sensitive to stellar emission.

The slope map is also nearly completely uniform - the ISM is hardly visible. The instrumental artifacts are also not present, possibly confirming the hypothesis that they are due to ORBS's struggles with handling low spectral resolution data. Once again, the galaxy is traced with the largest values in the error map. The simple explanation for this is that attempting to fit a two-parameter model to data best described with one-parameter will yield large errors. The background, sky emission has lower S/N and more scatter, allowing more freedom in the model that can be fit to the data. Of course, this does not mean the sky is best fit with an arbitrarily complex model, and these fits can be eliminated via the two statistical criteria. However, *there is the potential* to fit such a model to this noisy data. The galactic continuum in contrast is high S/N with less scatter, and large errors will be produced by trying to describe the continuum as

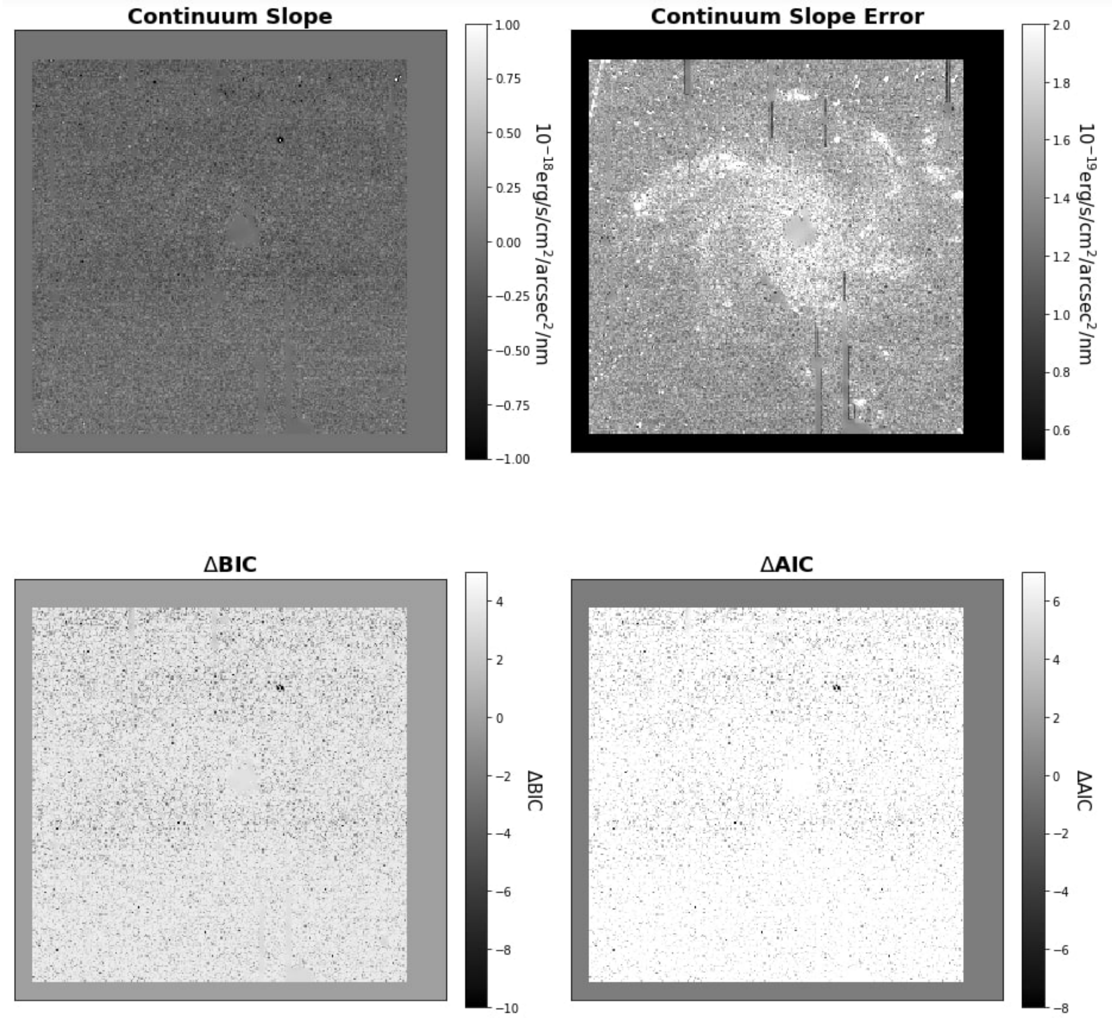

FIGURE 4.4: The same as Figure 4.3 but for the archival datacube. Once again, masked regions are interpolated using the surrounding pixels.

anything other than flat.

The goal of our analysis was to locate potential LE candidates via regions with statistically-significant negative slopes. This required a binned pixel to have a consistent negative slope within its error, as well as ΔBIC < -2 and ΔAIC < 0 to indicate that the two-parameter fit is significant. Out of 58954 binned pixels, only *six* met these criteria. Figure 4.5 shows the distribution of continuum slopes after each of the criteria were applied.

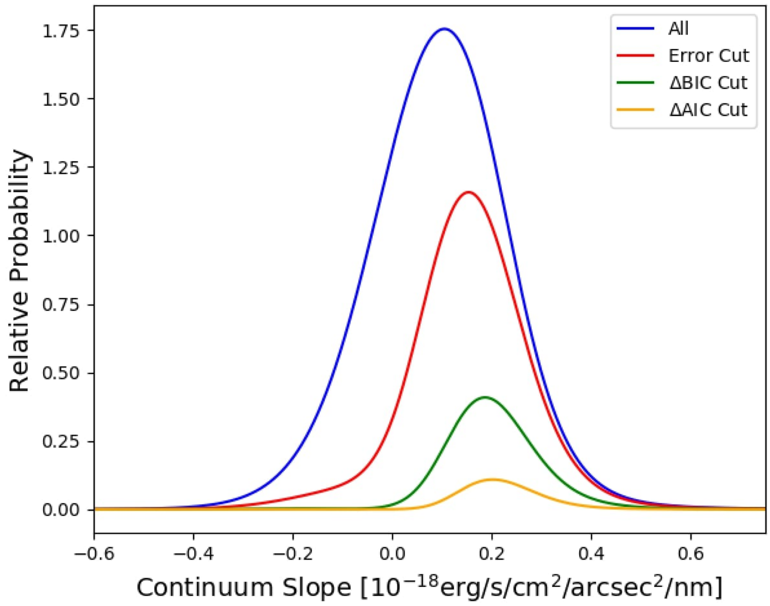

FIGURE 4.5: The distribution of continuum slopes after cuts in uncertainty, ΔBIC, and ΔAIC were applied. Each binned pixel is modelled as a Gaussian with the best fit two-parameter slope as the mean, and the fit uncertainty as the standard deviation.

The slopes begin evenly distributed about zero, as would be expected. As each cut is applied, it becomes subsequently less likely to find a pixel with a negative slope. The distribution even after the first cut in uncertainty is not quite bimodal, as more positively sloped regions remain than negative. However, there is still a tail extending into negative slopes. This end of the distribution may be influenced by instrumental effects in the manner discussed earlier - only the positive biases tend to be statistically significant. After the final cut in ΔAIC, the number of both positively and negatively sloped continua remaining is tiny. One is over an order of magnitude less likely to find a significant negative slope as opposed to a positive, and it is also around an order of magnitude less likely to find even a statistically significant positive value at a given continuum slope.

Our analysis has narrowed down the list of pixels housing potential LE candidates, and each of the six required further vetting to attempt to determine the cause of the negatively sloped continuum - be it the presence of a LE, or something else entirely.

4.2.1 Analysis of Potential Light Echo Candidates

First, each of the six regions were visually inspected to ensure that there were no obvious artifacts that could be causing the negative slope: emission from a nearby HII region for example. No obvious contamination was found in any of the pixels. A zoomed in map of the galaxy is shown in Figure 4.6, displaying the locations of the six areas.

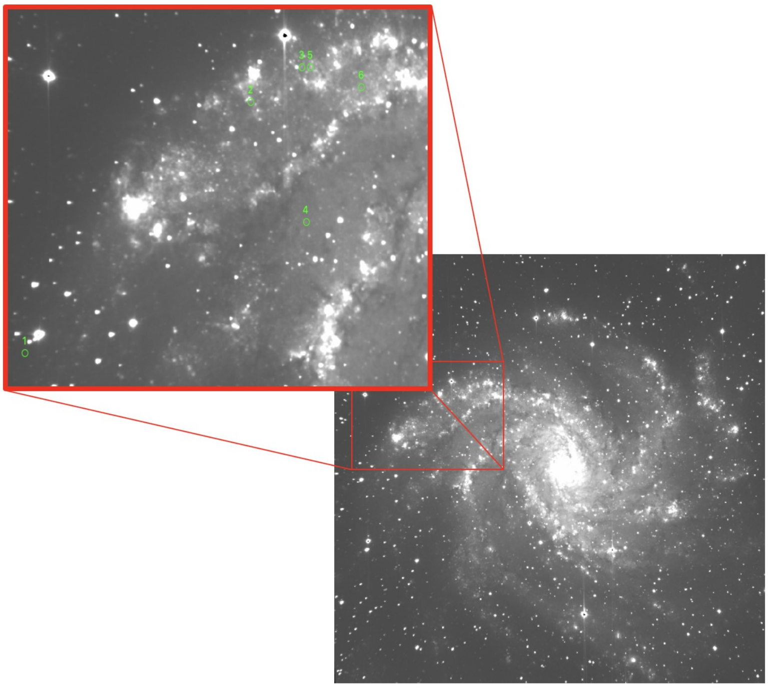

FIGURE 4.6: Zoomed in section of NGC 6946 showing the locations of the six binned pixels which met the LE candidate criteria. The region circles have been enlarged for visual clarity.

We note that each of these six regions lie very close to one another, and all positions are near the most negatively-biased of all the instrumental artifacts. Regions numbered 1, as well as 3 and 5 however, lie outside the edges of this negative artifact. Region #1 in fact, is within the most positively biased of all artifacts. It is unclear whether, or to what extent these results were influenced by the instrumental biases.

In order to determine the underlying cause of the negatively sloped continuum, the candidate pixels were compared with their local neighbourhoods - in an attempt to subtract out the dominant stellar continuum. An integrated spectra of the 35 binned pixels surrounding each candidate region was extracted, and scaled to the level of one binned pixel. This background spectrum was then subtracted from that of the candidate region yielding a 'difference spectrum'. These difference spectra would encapsulate the macroscopic deviations in each of the regions from their local neighbourhood, and hopefully help us determine the cause of the negatively-sloped continua. If the stellar continuum is roughly constant across the local neighbourhood of each region, the difference spectrum should be sensitive not to this stellar continuum, but to deviations from the local stellar continuum - perhaps the faint signature of a LE.

Such an analysis would not be possible on the data corrected with the laser calibration map, and was another reason why the laser calibration correction was not carried out on the full dataset. The artifacts introduced through this correction vary on single pixel scales, whereas the instrumental errors vary gradually over the span of $\sim$50 binned pixels. The instrumental artifacts should be roughly constant throughout the candidate region spectra and the background spectra, and should tend to cancel out in the difference spectra. The artifacts introduced by the laser calibration map correction change abruptly on scales smaller than the background regions. Therefore, we could not be confident that the difference spectra would be clear of all artifacts.

The properties of the difference spectra were once again determined by fitting the continuum. Table 4.2 summarizes the continuum fitting results for each of the six regions.

The difference spectra for each region must contain sufficient flux for a meaningful analysis to be completed. For each region, if the difference spectrum continuum level indicated by the one-parameter model best fit was negative, this indicated that there was insufficient flux to carry out any analysis. Three regions were not able to be further analyzed because of this reason. This does not conclusively rule out the presence of

TABLE 4.2: Continuum fitting results of the six candidate LE regions.

Region [1]	Continuum Slope (erg/s/cm^2/arcsec^2/nm)	ΔBIC	ΔAIC	S/N
1	-2.9(0.6)e-19	-12.3	-6.1	0.21
2	-	-	-	-
3	-	-	-	-
4	-2.0(0.4)e-19	-15.2	-9.8	2.69
5	-6(3)e-20	-2.2	3.2	2.80
6	-	-	-	-

Values in brackets are the error in the final decimal places, associated with each quantity.
- indicates continuum flux was negative and no meaningful analysis was performed.
[1] based on numbering in Figure 4.6.

a LE, it simply indicates that no LE can be identified brighter than the level of the background noise.

The remaining three difference spectra contain continuum levels at 0.21σ, 2.69σ, and 2.80σ respectively. This assumes a Gaussian model of background noise centred on 1.71×10^{-18} erg/s/cm^2/arcsec^2, which was fit to the flux distribution of sky pixels (e.g. Figure 4.7). The S/N of each continuum level was estimated by once again comparing the best fit one-parameter model to the mean noise level.

The continuum level of the first region is below the average noise level. Once again no further analysis can be performed as any features in the difference spectrum will not be able to be distinguished from noise. Region #5 has the highest S/N (at 2.8) of any of the difference spectra, however its ΔAIC does not meet our criterion, and therefore, we cannot claim that the excess emission present in this region is an ideal LE candidate.

The last region, Region #4 has a modest S/N of 2.7, a negative slope, and our statistical criteria indicate that the best fit two-parameter model is significant. Although it cannot be said for certain what the source of this emission is, this difference spectrum does meet all the criteria we determined for a LE candidate. We have identified an area of the galaxy with an excess of emission over its local neighbourhood, and the

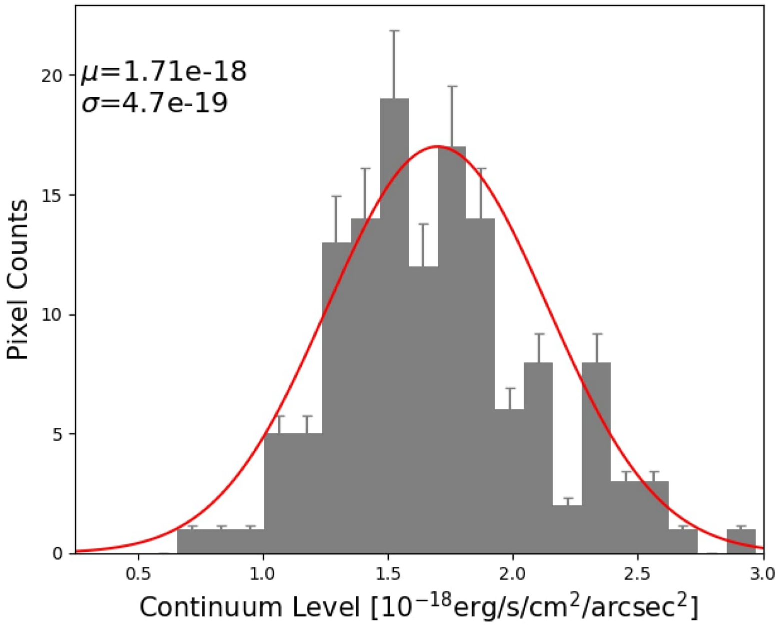

FIGURE 4.7: The distribution of flux in noise pixels, randomly sampled from 10 dark sky regions in the frame. The red curve is the best fit Gaussian model, and its parameters (μ, σ) are displayed.

excess emission displays the characteristics that we would expect for a SN LE. More observations of the entire P-Cygni profile, if there is indeed one in this spectrum, would be able to unequivocally confirm the presence of a LE. It should be noted that this region does lie within one of the negatively-biased instrumental artifacts. However, our approach in producing the difference spectrum should have minimized or negated the artifacts effect.

A model P-Cygni line profile was fit to the difference spectrum, and shown in Figure 4.8. The model P-Cygni profile has a maximum Hα flux of 6.2×10^{-18} erg/s/cm^2/arcsec^2, which would be at a 3.6σ level compared to noise. It also has a broadening of $\sim$3400 km/s, which is consistent with ejecta velocities in SNe. The difference spectrum is admittedly very noisy, and the χ^2 parameter for the P-Cygni fit is 3.0. If the P-Cygni is roughly approximated as a two-parameter model, the χ^2 cumulative probability distribution indicates that there is a 0.21 probability that the data representing the difference spectrum could be drawn from the model P-Cygni. This is not a complete confirmation of the

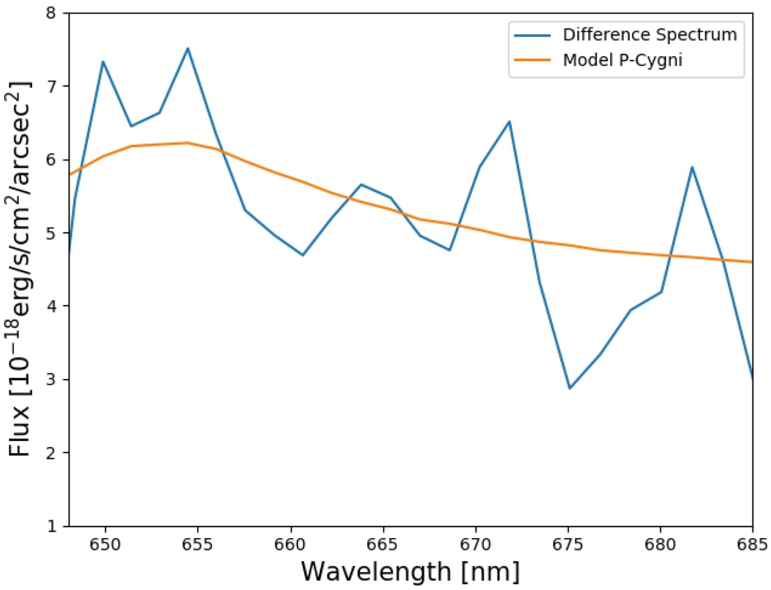

FIGURE 4.8: The difference spectrum of candidate LE region #4. A model P-Cygni profile has been fit to the difference spectrum for comparison. The P-Cygni profile peaks at a flux of 6.2×10^{-18} erg/s/cm^2/arcsec^2, as well as broadening of ~3400 km/s. The fit has a $\chi^2 = 3.01$.

model, nor is it a rejection. It is possible that a P-Cygni profile could explain the difference spectrum, however this is by no means unequivocal. Followup observations at both higher spectral and spatial resolution would be necessary to obtain a better understanding of this region and determine whether or not a LE from a SN older than a century is indeed present.

4.2.2 False Positive Calibration

Whether or not candidate region #4 contains a LE, our continuum-fitting method yielded six binned pixels meeting our LE criteria, out of 58954. If all six are false detections, then our method has a maximum false positive detection rate of 0.01%.

It is unclear exactly how much of an effect the instrumental artifacts have had here. Roughly half of the frame has slopes biased negative, and half positive. The six regions which met our criteria do all lie near the negatively-biased bands. If one considers that there may be other pixels in the frame which *would have* met out criteria, but did not because their slopes were biased positively, then the adjacent reasoning suggests that there will be a roughly equal number of pixels which only meet our criteria because of the negative bias on their slopes. There is no reason to suggest that this should not be symmetric; that many more pixels would be removed from the sample due to the positive bias, as would be added by the negative bias. Therefore, the number added and subtracted should be roughly equal and cancel out.

The six binned pixels, or 0.01%, is then a reasonable estimation of the false positive detection rate.

4.3 A Flux Limit for Light Echo Detection

Unfortunately, in part due to not obtaining our proposed observational depth, we did not manage to detect a large sample of LEs. Because of this, a firm limit in age and surface brightness leading to detectable LEs cannot be established. However, we can set an upper limit in peak Hα flux with the data we have available.

In order to establish an flux upper limit for LE detection, model P-Cygni profiles were inserted at random locations into the galaxy, and we attempted to detect them with our continuum slope method. Hα P-Cygni line profiles, with peak flux ranging from 0.5×10^{-17} to 2.0×10^{-16} erg/s/cm^2/arcsec^2 were tried. At each peak flux, 50 P-Cygni profiles were inserted into random locations in the galaxy. Our continuum fitting methodology was applied to each of the 50 regions to see how many times the continuum fit indicated the presence of a LE candidate. The fraction of 'LE detections' as a function of the peak Hα flux of the inserted model is shown in Figure 4.9. The entire process was repeated ten times, and the error bars shown represent the standard error in the mean detection fraction.

The detection fraction rapidly increases over the peak flux range of 0.2×10^{-16} to 0.75×10^{-16} erg/s/cm^2/arcsec^2. We consider our detection limit to be the point at which we recover the P-Cygni model 50% of the time. This occurs at a peak flux

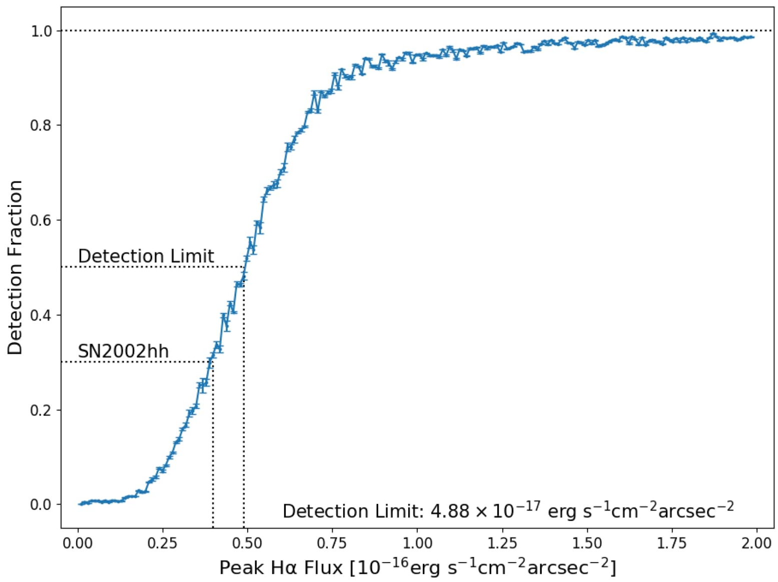

FIGURE 4.9: Detection rate of simulated LEs with increasing peak Hα brightness. Error bars are the standard error in the mean detection fraction when the process was repeated 10 times. We determine a flux limit of 5×10^{-17} erg/s/cm^2/arcsec^2 for LEs in our observations. LEs must be *at least* this faint in Hα or else they would have been detected in our analysis. The peak brightness of the SN 2002hh LE is shown for comparison - it falls below our detection limit. We would only detect LEs of this brightness 30% of the time.

of 5×10^{-17} erg/s/cm^2/arcsec^2. Therefore, any LEs present within NGC 6946 must be at least this faint in Hα, else we would have detected them in this work. The previous LE detection from SN 2002hh (e.g. Andrews et al., 2015) is also displayed in Figure 4.9 for comparison. This is the flux level that we had hoped to reach in our observations. However, at the depth of our observations, we would only recover LEs at the 2015 brightness of the SN 2002hh LE, 30% of the time. In our work, it falls about 1×10^{-17} erg/s/cm^2/arcsec^2 below our detection limit.

We believe that the analytical approach described in this section would benefit any future LE searches in NGC 6946. Such studies would need to reach at least the level of our detection limit in Hα in order to undertake a meaningful LE survey. However, it should be noted that approximately an order of magnitude in additional sensitivity would likely be necessary to establish a statistical distribution of LEs within NGC 6946.

Chapter 5

Conclusions

The major contribution of this thesis has been to develop a single observation, narrow-band spectroscopic method of identifying LE candidates, and test it on the largest known single-galaxy sample of Type II SNe. Using the narrow-band Hα filter, SN3, on the SITELLE IFTS, we observed the nearby spiral galaxy NGC 6946 for a total of four hours hoping to detect LEs from any of its ten known core-collapse SNe. Our method required fitting the continuum emission of regions throughout the galaxy, as highly-broadened P-Cygni Hα emission from a SN would appear to be negatively-sloped continuum in the narrow SN3 filter. Regions displaying such a slope would be ideal LE candidates.

As summarized by Sinnott (2013), one of the longstanding goals of the field of LE analysis has been to develop a single-observation LE detection method. Furthermore, in known LE samples Type II SNe are under-represented due to uncertainties in age and the range of their outburst luminosities - which are less luminous than thermonuclear SNe. Establishing a statistical sample of Type II SN LEs is also a critical endeavour.

Unfortunately, our survey yielded no LEs from the ten known SNe, and only one potential candidate from any SNe prior to 1917. Any detections were likely confounded in part by the lack of observation depth, we had proposed for and were granted a total of 12 hours of time, as well as large instrumental artifacts in the dataset for which there is no known solution. Nevertheless, we established an upper limit on LE Hα brightness of 5×10^{-17}erg/s/cm^2/arcsec^2 in this survey.

5.1 Possible Improvements to Our Methodology

Our study was very much affected by a lack of observation depth, as well as instrumental artifacts. If we had been able to observe for the full 12 hours that we were allotted, we likely would have been able to, at the very least, recover the previously discovered SN 2002hh LE. The major difficulty encountered in the data we received was the result of instrumental artifacts, possibly residuals from the phase calibration - caused in part by ORBS's inability to cope with low spectral resolution data. However, the reasons for these software and hardware issues are not completely understood. SITELLE is primarily used for high spectral resolution studies, and we have obtained the first ever observations with SITELLE at such a low spectral resolution. As such, our data is the only set available on which these artifacts can be studied. Issues related to software modelling limitations may be rectified in later releases of ORBS.

The width of the SN3 filter was both a help and a hinderance for this study. Although its narrow bandpass allowed us to approximate a P-Cygni profile as a single negative slope, fitting the entire P-Cygni profile would lead to a more unequivocal detection. Unfortunately, SITELLE has no filter which captures the absorption component of the P-Cygni. A wide filter, for example the r$'$ of Gemini GMOS, would be needed to capture the entire P-Cygni profile and confirm the presence of a LE. A wider SITELLE Hα filter would allow for detection, and confirmation of a candidate LE in a single observation. Short of that, the same length of observations in the neighbouring SITELLE filter, C2, would provide better characterization of the stellar continuum. C2 falls outside the range of the highly-broadened Hα line, and deviations in the continuum from C2 to SN3 would provide stronger evidence that negatively-sloped continua are due to a LE.

In striving for the deepest possible observations, we likely also sacrificed too much in spectral resolution. Our chosen resolution resulted in only 13 frames encompassing the entirety of the continuum emission in the SN3 filter. The prominent emission lines, Hα, [NII]654.8, 658.4, and [SII]671.7, 673.1 were combined into two broad, unresolved groups, and so could not be individually subtracted. Our low spectral resolution effectively 'smeared' the emission lines out over a wider wavelength range. For example, the peaks of the [SII] doublet are separated by only 1.4 nm, however in our observations, emission from the doublet is seen in frames covering wavelengths from 668 to 676 nm. The 1.4 nm gap has been spread to ∼8nm. Conversely, in the archival cube the [SII] doublet appears in frames spanning 671 to 675 nm - only half the spread present in our data.

As previously discussed, increasing the spectral resolution would not change the number of frames lying outside the filter bandpass, but it does change the amount that emission lines are 'smeared' into neighbouring frames. The spectral resolution essentially acts as a source of instrumental broadening - causing the [SII] doublet to be spread over 8 nm in our observations, but only 4 nm in the archival cube.

SITELLE does introduce additional broadening through its sine cardinal line shapes. Very strong emission lines, such as Hα, will have prominent side-lobes in IFTS data; something that can be seen clearly in Figure 3.2. The strongest emission lines will always spill into neighbouring continuum frames because of these side-lobes, but the effect is a strong function of line strength, and is nearly negligible for the weaker [SII] lines.

With these considerations, a spectral resolution of at least R = 600 would likely be ideal for a future SITELLE survey. This would provide enough resolution to at least differentiate the individual emission lines in the two groups, and limit the maximum instrumental broadening. At this resolution, not only would we have double the number of frames spanning the SN3 continuum, but a few additional frames would also be gained by limiting the instrumental broadening of the [SII] doublet. No frames are likely to be gained from the Hα and [NII] complex with SITELLE due to the prominence of the Hα side-lobes, which will increase in strength as the emission becomes more concentrated in a smaller number of frames.

Increasing the number of continuum frames will eliminate much of the large and seemingly random variations seen in the continuum as it converges to its true underlying distribution. Higher spectral resolution will also aggregate the emission lines into fewer frames, allowing for easier subtraction, as well as make for easier identification and correction of the sky lines at the edge of the filter.

Moreover, R = 600 is not so high of a spectral resolution such that the S/N we could hope to reach is detrimentally affected. By increasing the number of spectral elements, the number of photons per spectral element will naturally decrease. Therefore, the S/N per spectral element will also decrease. For sky limited, or bright sources the net effect is to reduce the S/N by a factor of $\frac{1}{\sqrt{2}}$ for each factor of two in binning. By increasing our spectral resolution from R = 300 to R = 600, we are effectively dividing each spectral element in two, and suffering the equivalent penalty in S/N. For example, based on outputs of the SITELLE exposure time calculator (ETC) [1], with our initial observing parameters we would see a LE at the brightness of the Andrews et al. (2015) detection of the SN 2002hh LE with a S/N of ∼1.5. With a spectral resolution of R = 600 and the same total length of observations, we would still reach a S/N of ∼1.1, but will more than double the number of frames to which a P-Cygni profile can be fit. Increasing the total observation time by an additional three hours would allow us to reach the same S/N as with R = 300.

The spatially-resolved IFU spectroscopy of SITELLE was key to this study, but similar instruments can also be used in future work. In fact, more well-behaved and well-understood IFUs may actually be superior to using the SITELLE IFTS. Our work encountered numerous data reduction and instrumental difficulties, caused in part by the increased complexity of an IFTS setup as opposed to a slit or fibre spectrograph, as well as 'growing pains' associated with SITELLE being a relatively new instrument. Our study was the first to use SITELLE at such a low spectral resolution, and our instrumental artifacts are likely due to the current inability of ORBS to accurately recombine the two interferograms from the two CCDs. As SITELLE garners an increased user-base,

[1] http://etc.cfht.hawaii.edu/sit/

its complexities and complications will become better understood, and more easily corrected. Instrument characterization is one of the major benefits of using an established instrument over a new one - data products are generally artifact-free, and reduction kinks have been already solved. In this manner, our observations were meritorious for the development of SITELLE.

5.2 Future Work - The MUSE Spectrograph

A particular instrument that could be significant in future LE studies is MUSE (Multi Unit Spectroscopic Explorer), operated by the European Space Agency (ESO) on the 8 m VLT (Very Large Telescope) in Chile (Bacon et al., 2010). MUSE offers continuous spectral coverage from 465 to 930 nm, allowing access to both the absorption and emission components of an Hα P-Cygni line, and eliminate the degeneracies that we have had to circumvent in observing only the down-sloping side of the emission line.

MUSE reaches a spectral resolution of 1750 at 450 nm, and increases roughly linearly to 3750 at 930 nm. At a wavelength of 656.6 nm MUSE reaches R = 2500, yielding nearly 0.25 nm resolution. Unlike SITELLE, this resolution is fixed, and is independent of the length of observations proposed. This could be both a benefit, and a hinderance to searches for LEs. R = 2500 is over four times greater than the ideal resolution which we have suggested for future LE searches - meaning the individual emission lines which contaminate a P-Cygni Hα line profile will be nearly perfectly resolved, and can be isolated and subtracted. However, having four times more spectral elements will result in an effective reduction of S/N by a factor of two. Of course, after the removal of the individual emission lines, the continuum emission can be binned down to the desired spectral resolution in order to offset losses in S/N.

The main tradeoff in choosing MUSE is the smaller FOV: $1' \times 1'$ in Wide Field Mode (WFM) compared to $11' \times 11'$ with SITELLE. Both instruments have comparable spatial sampling: 0.32″ for SITELLE and 0.2″ for MUSE - with Adaptive Optics (AO), however, MUSE has a well characterized 0.35″ PSF providing a stark improvement over the currently distorted ∼2″ PSF of SITELLE (Richard & Bacon, 2019). In addition, MUSE offers a Narrow Field Mode (NFM) also with AO. The FOV is decreased to 7.4″×7.4″ - still large enough to resolve LEs - but the spatial sampling is upgraded to 0.025″/pixel, and the spatial resolution achieved can reach up to 55 mas (Richard & Bacon, 2019).

It is extremely rare for large-field LE searches to be undertaken, for reasons already discussed. More often, searches are conducted over a more restrictive area, looking for LEs from known events. In such cases, SITELLE's large FOV can easily be replaced by that of MUSE. The spatial resolution of MUSE will outperform SITELLE by being able to resolve LEs closer to the SN outburst, and limit contamination of the LE search areas by neighbouring HII regions - factors that were large hinderances to our SITELLE-based LE search. For example, based on Table 4.1, with the 0.35″ PSF of MUSE's WFM, LEs from all SNe with the exception of SN 2017eaw would be resolvable. With NFM, even LEs from SN 2017eaw could be resolved. With SITELLE's distorted PSF, only LEs from SNe prior to 1980 could reasonably be resolved.

The light collecting potential of MUSE on the VLT has both benefits and detriments when compared to SITELLE. MUSE is mounted on an 8 m telescope, as compared to the 3.6 m CFHT on which SITELLE is mounted. Mirror size alone would provide a factor of 2.2 increase in S/N for MUSE for a given exposure time. However, the throughput of MUSE in the Hα regime is only 35% for WFM and 26% for NFW, compared with nearly 95% for SITELLE (Richard & Bacon, 2019, Drissen, 2016). These pros and cons can be quantified by the respective ETC for each instrument. We simulated observations of an Hα P-Cygni line, with a flux of 3×10^{-17}erg/s/cm^2/arcsec^2, and broadening of $\sim$ 40nm - parameters of the Andrews et al. (2015) detection. For SITELLE, with 12 hours of observations at R = 600, we reach a S/N of 1.1. For MUSE, the S/N is 0.48 for WFM, and only 0.02 for NFM. If the MUSE data is binned down to R = 600, the

S/N is increased to 0.96 and 0.1 respectively. SITELLE clearly outperforms MUSE in this category, but as already discussed, MUSE has other benefits which cannot be taken into account in a simple S/N calculation.

To attempt to quantify the differences between the two instruments, we created a Figure of Merit which encapsulates changes in S/N, as well as both spectral and spatial resolution. Our Figure of Merit, formulated in Equation 5.1, describes the effective depth at which we could potentially detect LE candidates for MUSE as compared to SITELLE.

$$\text{FoM} = \frac{\text{Detection Limit}}{(\text{S/N})(\text{Coverage})} \tag{5.1}$$

The *Detection Limit*, as we identified earlier for SITELLE, is an estimate of the faintest LEs which would be recovered by our methodology. Our Figure of Merit weights this limit by the S/N that each instrument could reach for a given line flux, and by the effective spatial *Coverage* of each instrument. In our case, SITELLE could only resolve LEs from six of ten SNe in NGC 6946, whereas MUSE's WFM could resolve nine, and NFM, all ten. *Coverage* would then be 0.6, 0.9 and 1.0 respectively. The S/N for each case, is that which was simulated by the ETC.

For SITELLE, the *Detection Limit* is simply what we found in Chapter 4.3. With MUSE, the *Detection Limit* must be adjusted to account for the fact that more continuum points will be available due to the higher spectral resolution, and that the entire P-Cygni profile will be visible. In our methodology, the detection of a P-Cygni profile is dependent on the values of the statistical criteria calculated. For the ΔBIC, and similarly for the ΔAIC, the value varies with the number of data points, n, and the variances of the data compared to the one-parameter, σ_{1P}, and two-parameter, σ_{2P}, fits as:

$$\Delta\text{BIC} = \text{n} \ln\left(\frac{\sigma_{\text{2P}}}{\sigma_{\text{1P}}}\right) + \text{n} \tag{5.2}$$

If $\sigma_{2\mathrm{P}} \leq 0.37\sigma_{1\mathrm{P}}$, then the ΔBIC parameter decreases linearly with each additional data point added to the set. The significance of this is as follows: if the variance of the two-parameter fit is sufficiently small compared to that of the one-parameter fit, then by adding more data points the ΔBIC parameter indicates an increasingly statistically significant two-parameter fit.

In the cases of four of the six potential LE regions discussed in Chapter 4.2.1, the variances met the above criterion. Therefore, if additional continuum points were available to be fit, the result would be a lower ΔBIC, and by the same logic a lower ΔAIC - *stronger* evidence for a P-Cygni profile. This assumes that the variances remain constant as data points are added, but if the underlying distribution truly is a P-Cygni profile, additional data should decrease the two-parameter variance, while increasing the one-parameter variance, thereby reducing the statistical criteria further.

To make this quantitative, consider that MUSE data is initially observed at a spectral resolution of R = 2500 in the regime of Hα, however as proposed earlier, it can be binned down to R = 600 to increase S/N. The 34 nm extent of the SN3 filter would be covered in MUSE data at R = 600 by a total of 33 frames. The emission lines could be subtracted at the highest spectral resolution, leaving the binned spectrum relatively free of nebular emission. However, supposing the worst case scenario, and the same number of frames are contaminated by emission lines in the binned MUSE spectrum, as in our SITELLE data, then only eight frames would need to be removed. This still leaves the MUSE spectrum with 25 continuum frames, nearly double what we had.

Let's consider the effect this would have on Region #4 in Chapter 4.2.1; the sole LE candidate identified. Within this region, we calculated variances such that $\sigma_{2\mathrm{P}} = 0.32\sigma_{1\mathrm{P}}$. Therefore, if 25 instead of 13 data points were available in the fit of the aforementioned Region #4, its ΔBIC parameter would have been -18.7, instead of -15.2; a decrease of 3.5.

To connect this to the Figure of Merit calculation, it was found while determining the detection limit in our study that every increase of 1×10^{-18}erg/s/cm^2/arcsec^2 in peak P-Cygni flux had an accompanying decrease of 0.3 in the ΔBIC. With the extra data, Region #4 would effectively have the ΔBIC of a P-Cygni profile brighter by 1.2×10^{-17}erg/s/cm^2/arcsec^2. In effect, MUSE's additional data points allow us to probe for LEs at a greater depth, thereby reducing the detection limit.

The above calculation does not include the benefit of being able to sense full extent of the P-Cygni profile as opposed to the one segment available in the SN3 filter. The ability to identify not only the downslope of the emission component, but of the absorption component as well, makes it roughly twice as easy to identify LE candidates; effectively probing twice as deep. Consider then, the following estimated *Detection Limit* for MUSE data: the twelve extra data points would provide an additional 1.2×10^{-17}erg/s/cm^2/arcsec^2 in sensitivity, on top of the factor of two gained from observing the entire P-Cygni profile. Therefore, with MUSE we could potentially identify LE candidates down to a limit of 2×10^{-17}erg/s/cm^2/arcsec^2.

We are now in a position to evaluate the Figure of Merit for the two instruments - the constituent parameters are summed up in Table 5.1. Comparing the four observing modes, WFM provides three times greater sensitivity over SITELLE at R = 300, and 2.5 times more compared to R = 600. NFM performs the worst for the same length of observations. NFM's ability to detect LEs is greatly effected by its low throughput, leading to a much decreased S/N compared to the other two observing modes. WFM however shows marked improvement over both resolutions of SITELLE observations. Observing with SITELLE at R = 600 would have a slight improvement over R = 300, but would still not be able to probe the depths that would likely be available to MUSE.

Table 5.1: Figures of Merit Comparing MUSE and SITELLE

Instrument	Detection Limit	S/N	Coverage	Figure of Merit
SITELLE R=300	4.9×10^{-17}	1.4	0.6	6×10^{-17}
SITELLE R=600	3.6×10^{-17}	1.1	0.6	5×10^{-17}
MUSE WFM	1.9×10^{-17}	1	0.9	2×10^{-17}
MUSE NFM	1.9×10^{-17}	0.1	1.0	2×10^{-16}

MUSE Figures of Merit are calculated assuming spectra are binned to R=600.

5.2.1 Potential Observing Strategies

Single Galaxy LE Searches

Due to practical limits on declination (the VLT is located in northern Chile) MUSE will never be able to observe NGC 6946, so the opportunity for us to carry out an identical study is non-existent. Fortunately, there are a number of galaxies visible in the southern sky that contain multiple SNe and which would be suitable targets. One of the most prominent is the easily observable LMC, which contains SN 1987A. Observations of some of the readily detectable LEs associated with SN 1987A would prove a useful endeavour to further calibrate our methodology.

A selection of the closest and most prolific galaxies for SNe are shown in Table 5.2. Each are close enough to allow for spatially resolved spectroscopy, as well as contain at least four SNe, evenly spread over a period of 50 or more years. As such, each of these galaxies could potentially contain a statistical distribution of resolvable LEs with MUSE's enhanced capabilities.

The most promising target is the nearby galaxy M83, at a distance of 4.66 Mpc (Tully et al., 2016). M83 has had six Type II SNe since 1923, and even the most recent SN, 1983N, could potentially have produced LEs with an angular separation of 3.5 arcseconds - certainly resolvable with MUSE's spatial resolution (Gal-Yam et al., 2013). The major downside to observations of M83 is the combination of distance, and MUSE's FOV. At only 4.66 Mpc, M83 has an angular size of $12.9' \times 11.5'$ - too large to even fit in SITELLE's

TABLE 5.2: Potential Single Galaxy MUSE Targets

Name	Declination	Distance (Mpc)	Number of SNe
M61	$+04°28'25''$	16.1	7
M83	$-29°51'57''$	4.7	6
NGC 2207	$-21°22'22''$	24.9	6
NGC 1084	$-07°34'42''$	20.5	5
NGC 4038	$-19°52'10''$	13.8	5
NGC 1365	$-36°8'25''$	17.2	4
NGC 1559	$-62°47'1''$	19.2	4

Declinations and distances are from NASA/IPAC Extragalactic Database and references therein.

FOV. This means at least five exposures of M83 would have to be observed in order to capture all six SNe (SNe 1983N and 1945B are separated only by $\sim 45''$ and could be captured in the same exposure).

Another more distant, but still SN-rich target is NGC 4038. Aside from the presence of SNe, NGC 4038 is interacting with NGC 4039 in a system often called the Antenna Galaxies (Barnes & Hernquist, 1992). At 13.8 Mpc, NGC 4038 has an angular size of only $5.2'\times3.1'$. It would only require two pointings to observe, since SNe 1921A, 1974E, and 2004gt lie within less than an arcminute of each other, as do SNe 2007sr and 2013dk. Observations of the Antenna galaxies would also be meritorious to the study of interacting galaxies and star formation.

Multiple Target Samples

Unfortunately, the amount of dust varies dramatically from SN to SN, even within the same galaxy. There is no guarantee that two SNe will have a comparable amount of dust in their immediate neighbourhood just by nature of being located in the same galaxy. The understanding of the variance in dust density in distant galaxies is an uncertainty that we are unlikely to ever be able to reduce, and it is therefore no guarantee that a SN-rich galaxy will produce many LEs. Furthermore, all of the galaxies listed in Table 5.2 would require multiple MUSE pointings in order to image the surroundings of each of their SNe. A more practical observing strategy may be to target multiple closer galaxies with one, or two SNe, in order to build up a statistical sample of LEs.

M83 still remains a good target for this type of survey - as mentioned earlier, due to its proximity it would need multiple pointings to observe all of its SNe. Since M83 has not had any SNe since 1983, this sample could be supplemented with observations of NGC 2403 at a distance of 2.5 Mpc. NGC 2403 has had two Type II SNe: 1954J and 2004dj. SN 2004dj is notable as being the brightest SN since SN 1987A at the time of its discovery, with an apparent magnitude of 11.2 (Vinkó et al., 2006).

This work has provided a methodology to enable LE candidate identification in single-observation spectroscopic data, however the ideal combination of instrument and target has yet to be identified. We have taken steps to resolve the largest remaining problem in the study of LEs - the development and observation of a program to identify a statistical sample of LEs, and set firm detection limits. A revisiting of this work, when the flaws in SITELLE's data analysis techniques are better understood, may yet prove the most fruitful route to this goal. In the near future however, observations with MUSE of some of the targets suggested above are likely to be a better opportunity to identify and study LEs.

Bibliography

Akaike, H. 1973, Biometrika, 60, 255

Anand, G. S., Rizzi, L., & Tully, R. B. 2018, The Astronomical Journal, 156, 105

Anderson, D., & Burnham, K. 2004, Second. NY: Springer-Verlag, 63

Andrews, J. E., Smith, N., & Mauerhan, J. C. 2015, Monthly Notices of the Royal Astronomical Society, 451, 1413

Arenou, F., Grenon, M., & Gomez, A. 1992, Astronomy and Astrophysics, 258, 104

Arnett, D., Fryxell, B., & Mueller, E. 1989, The Astrophysical Journal, 341, L63

Arnett, W., & Truran, J. 1969, The Astrophysical Journal, 157, 339

Bacon, R., et al. 2010, in Ground-based and Airborne Instrumentation for Astronomy III, Vol. 7735, International Society for Optics and Photonics, 773508

Barbon, R., Buondi, V., Cappellaro, E., & Turatto, M. 1999, Astronomy and Astrophysics Supplement Series, 139, 531

Barkat, Z., Rakavy, G., & Sack, N. 1967, Physical Review Letters, 18, 379

Barlow, M., et al. 2005, The Astrophysical Journal Letters, 627, L113

Barnes, J. E., & Hernquist, L. 1992, Annual review of astronomy and astrophysics, 30, 705

Beals, C. 1932, Monthly Notices of the Royal Astronomical Society, 92, 677

Beals, C. S. 1953, Publications of the Dominion Astrophysical Observatory Victoria, 9, 1

Bionta, R., et al. 1991, in Neutrinos And Other Matters: Selected Works of Frederick Reines (World Scientific), 340

Blanco, W., et al. 1987, The Astrophysical Journal, 320, 589

Blondin, S. 2018, Stéphane blondin - graphics

Boffi, F. R., Sparks, W. B., & Macchetto, F. D. 1999, Astronomy and Astrophysics Supplement Series, 138, 253

Boomsma, R., Oosterloo, T., Fraternali, F., Van Der Hulst, J., & Sancisi, R. 2008, Astronomy & Astrophysics, 490, 555

Botticella, M. T., et al. 2009, Monthly Notices of the Royal Astronomical Society, 398, 1041

Burbidge, E. M., Burbidge, G. R., Fowler, W. A., & Hoyle, F. 1957, Reviews of modern physics, 29, 547

Burnham, K. P., Anderson, D. R., & Huyvaert, K. P. 2011, Behavioral ecology and sociobiology, 65, 23

Canal, R., & Schatzman, E. 1976, Astronomy and Astrophysics, 46, 229

Cappellaro, E., Evans, R., & Turatto, M. 1999, arXiv preprint astro-ph/9904225

Carroll, B. W., & Ostlie, D. A. 2017, An introduction to modern astrophysics (Cambridge University Press)

Cavanaugh, J. E. 1997, Statistics & Probability Letters, 33, 201

Claeskens, G., & Hjort, N. L. 2008, Model selection and model averaging, Technical report, Cambridge University Press

Couderc, P. 1939, in Annales d'Astrophysique, Vol. 2, 271

Crotts, A. P., & Kunkel, W. E. 1991, The Astrophysical Journal, 366, L73

Crotts, A. P., Kunkel, W. E., & McCarthy, P. J. 1989, The Astrophysical Journal, 347, L61

Davidson, K., & Humphreys, R. M. 1997, Annual Review of Astronomy and Astrophysics, 35, 1

De Groot, M. 1969, Bulletin of the Astronomical Institutes of the Netherlands, 20, 225

Dey, A., & Valdes, F. 2014, Publications of the Astronomical Society of the Pacific, 126, 296

Diehl, R., et al. 2006, Nature, 439, 45

Dray, L. M., Tout, C. A., Karakas, A. I., & Lattanzio, J. C. 2003, Monthly Notices of the Royal Astronomical Society, 338, 973

Drissen, L. 2016, SITELLE: A Primer (2.0 ed.), Universite Laval, CFHT

Drissen, L., Bernier, A.-P., Rousseau-Nepton, L., Alarie, A., Robert, C., Joncas, G., Thibault, S., & Grandmont, F. 2010, in Ground-based and Airborne Instrumentation for Astronomy III, Vol. 7735, International Society for Optics and Photonics, 77350B

Drory, N., et al. 2015, The Astronomical Journal, 149, 77

Dwek, E. 1983, The Astrophysical Journal, 274, 175

Fabian, A. C. 2008, science, 320, 1167

Filippenko, A. V. 2004, arXiv preprint astro-ph/0412029

Fryer, C. L., & Kalogera, V. 2001, The Astrophysical Journal, 554, 548

Gal-Yam, A., Mazzali, P., Manulis, I., & Bishop, D. 2013, Publications of the Astronomical Society of the Pacific, 125, 749

Gordon, R. A. 2015, Regression analysis for the social sciences (Routledge)

Habets, G., & Heintze, J. 1981, Astronomy and Astrophysics Supplement Series, 46, 193

Hamuy, M., & Pinto, P. A. 2002, The Astrophysical Journal Letters, 566, L63

Hillebrandt, W., & Niemeyer, J. C. 2000, Annual Review of Astronomy and Astrophysics, 38, 191

Hirata, K., et al. 1987, Physical Review Letters, 58, 1490

Humphreys, R. 1978, The Astrophysical Journal, 219, 445

Hyman, S. D., van Dyk, S. D., Weiler, K. W., & Sramek, R. A. 1995, The Astrophysical Journal, 443, L77

Kapteyn, J. 1901, Astronomische Nachrichten, 157, 201

Kasen, D., Woosley, S., & Heger, A. 2011, The Astrophysical Journal, 734, 102

Kass, R. E., & Raftery, A. E. 1995, Journal of the american statistical association, 90, 773

Kim, S.-W., & Chun, M.-S. 1984, Journal of Korean Astronomical Society, 17, 23

Kirshner, R. P., Oke, J., Penston, M., & Searle, L. 1973, The Astrophysical Journal, 185, 303

Kotak, R., et al. 2009, The Astrophysical Journal, 704, 306

Krause, O., Birkmann, S. M., Usuda, T., Hattori, T., Goto, M., Rieke, G. H., & Misselt, K. A. 2008a, Science, 320, 1195

Krause, O., Tanaka, M., Usuda, T., Hattori, T., Goto, M., Birkmann, S., & Nomoto, K. 2008b, Nature, 456, 617

Ledrew, G. 2001, Journal of the Royal Astronomical Society of Canada, 95, 32

Li, W., et al. 2011, Monthly Notices of the Royal Astronomical Society, 412, 1441

Liu, Q. 2019, Private Communication

Luo, D., & McCray, R. 1991, The Astrophysical Journal, 379, 659

Martin, T., Drissen, L., & Joncas, G. 2015, in Astronomical Data Analysis Software an Systems XXIV (ADASS XXIV), Vol. 495, 327

Martin, T. B., Drissen, L., & Melchior, A.-L. 2017, Monthly Notices of the Royal Astronomical Society, 473, 4130

Martin, T. B., Prunet, S., & Drissen, L. 2016, Monthly Notices of the Royal Astronomical Society, 463, 4223

McDonald, B. J. 2012, Master's thesis, McMaster University

McQuarrie, A. D., & Tsai, C.-L. 1998, Regression and time series model selection (World Scientific)

Meikle, W. P. S., et al. 2006, The Astrophysical Journal, 649, 332

Misra, K., Pooley, D., Chandra, P., Bhattacharya, D., Ray, A. K., Sagar, R., & Lewin, W. H. 2007, Monthly Notices of the Royal Astronomical Society, 381, 280

Miville-Deschênes, M.-A., & Lagache, G. 2005, The Astrophysical Journal Supplement Series, 157, 302

Nomoto, K. 1987, The Astrophysical Journal, 322, 206

Nugent, P. E., et al. 2011, Nature, 480, 344

Oaster, L. 2008, Master's thesis, McMaster University

Osterbrock, D. E., Fulbright, J. P., Martel, A. R., Keane, M. J., Trager, S. C., & Basri, G. 1996, Publications of the Astronomical Society of the Pacific, 108, 277

Patat, F. 2005, Monthly Notices of the Royal Astronomical Society, 357, 1161

Perlmutter, S., et al. 1999, The Astrophysical Journal, 517, 565

Phillips, M. M. 1993, The Astrophysical Journal, 413, L105

Prieto, J. L., et al. 2008, The Astrophysical Journal Letters, 681, L9

Prunet, S. 2019, private communication

Rest, A., et al. 2011, The Astrophysical Journal, 732, 3

Rest, A., et al. 2012, Nature, 482, 375

Rest, A., et al. 2005, Nature, 438, 1132

Rest, A., et al. 2008, The Astrophysical Journal Letters, 681, L81

Richard, J., & Bacon, R. 2019, MUSE User Manual (7.3 ed.), ESO

Riess, A. G., et al. 1998, The Astronomical Journal, 116, 1009

Ritchey, G. W. 1901, The Astrophysical Journal, 14

Rosino, L. 1971, Information Bulletin on Variable Stars, 515

Rousseau-Nepton, L., Robert, C., Martin, R., Drissen, L., & Martin, T. 2018, Monthly Notices of the Royal Astronomical Society, 477, 4152

Sahu, D. K., Anupama, G., Srividya, S., & Muneer, S. 2006, Monthly Notices of the Royal Astronomical Society, 372, 1315

Schaefer, B. E. 1987, The Astrophysical Journal, 323, L47

Schinnerer, E., Böker, T., Emsellem, E., & Lisenfeld, U. 2006, The Astrophysical Journal, 649, 181

Schlegel, E. M. 1994, x-ray emission from the historical supernovae in the spiral galaxy ngc 6946: Sn1980k and sn1968d recovered?, Technical report, SCAN-9411090

Schwarz, G., et al. 1978, The annals of statistics, 6, 461

Seeger, P. A., Fowler, W. A., & Clayton, D. D. 1965, The Astrophysical Journal

Sinnott, B. 2013, Ph.D. thesis, McMaster University

Sinnott, B., Welch, D., Rest, A., Sutherland, P., & Bergmann, M. 2013, The Astrophysical Journal, 767, 45

Smartt, S. J. 2009, Annual Review of Astronomy and Astrophysics, 47, 63

Smith, N., et al. 2009, The Astrophysical Journal Letters, 697, L49

Sparks, W. 1994, The Astrophysical Journal, 433, 19

Stanishev, V., Pastorello, A., & Pursimo, T. 2008, Central Bureau Electronic Telegrams, 1235

Struve, O. 1935, The Astrophysical Journal, 81, 66

Sugerman, B. E. 2003, The Astronomical Journal, 126, 1939

Sugerman, B. E., et al. 2012, The Astrophysical Journal, 749, 170

Tully, R. B., Courtois, H. M., & Sorce, J. G. 2016, The Astronomical Journal, 152, 50

Tylenda, R. 2004, Astronomy & Astrophysics, 414, 223

Van Kerkwijk, M. H., Chang, P., & Justham, S. 2010, The Astrophysical Journal Letters, 722, L157

Vinkó, J., et al. 2006, Monthly Notices of the Royal Astronomical Society, 369, 1780

Wampler, E. J., Wang, L., Baade, D., Banse, K., D'Odorico, S., Gouiffes, C., & Tarenghi, M. 1990, The Astrophysical Journal, 362, L13

Welch, D., Clayton, G., & Sugerman, B. 2008, Central Bureau Electronic Telegrams, 1330

Welch, D., Clayton, G. C., Campbell, A., Barlow, M., Sugerman, B. E., Meixner, M., & Bank, S. 2007, The Astrophysical Journal, 669, 525

Wenger, M., et al. 2000, Astronomy and Astrophysics Supplement Series, 143, 9

Wesson, R., et al. 2010, Monthly Notices of the Royal Astronomical Society, 403, 474

West, R., Lauberts, A., Jorgensen, H., & Schuster, H. 1987, Astronomy and Astrophysics, 177, L1

Whelan, J., & Iben Jr, I. 1973, The Astrophysical Journal, 186, 1007

Whipple, F. L. 1939, Proceedings of the National Academy of Sciences of the United States of America, 25, 118

Woosley, S. E., Heger, A., & Weaver, T. A. 2002, Reviews of modern physics, 74, 1015

Xu, J., Crotts, A. P., & Kunkel, W. E. 1994, The Astrophysical Journal, 435, 274

Young, T. R., & Branch, D. 1989, The Astrophysical Journal, 342, L79